APPENDIX D: TEST SITE PORTFOLIOS

SITES 0, 1, 2, 3, AND 4A: MDOT US-23 AGGREGATE TEST SITE

INTRODUCTION

The cores received from the MDOT US-23 Aggregate Test Site are from pavements in good condition constructed in the years 1993 and 1994. The cores represent pavements with five different coarse aggregate types: two carbonate sources, two natural gravel sources, and one blast furnace slag source. Table D-1 summarizes the mix design information for the five sites. Figure D-1 depicts the mix volumetrics for the five sites. From Table D-1 and Figure D-1, it is apparent that coarse aggregate type is not the only variable that changed between the different mixture designs. For example, the water to cementitious ratio (*w/cm*) varies from 0.41 to 0.49, and, the volumes of aggregate vary considerably. The pavements with natural gravel contain considerably less fine aggregate, and the pavement with slag contains considerably more fine aggregate. However, the cement paste volumes remain relatively constant between the five sites.

To investigate the sites, slabs were cut from the cores in a plane perpendicular to the pavement surface. Some of the slabs were polished and used for chemical staining and stereo OM, other slabs were cut into billets and prepared in thin section, and the rest of the slabs were crushed into powder to perform chemical extractions. Figures D-2 through D-6 are provided to give a general overview of the different pavements. It is interesting to note that the interface with the cement paste appears different for some of the coarse aggregate types. In the carbonate-bearing pavements, there is often a light colored zone in the cement paste surrounding the coarse aggregate, and sometimes the coarse aggregates have darkened rims in contact with the cement paste. In the slag-bearing pavement, there is often a dark colored zone in the cement paste surrounding the coarse aggregate.

CHEMICAL STAINING

A solution of sodium cobaltinitrite was applied to the polished slab surfaces to stain potassium-bearing alkali-silica gels yellow. The alkali-silica gel stain primarily affected the chert and siltstone constituents of the fine aggregate common to the five sites. Figure D-7 shows and example of a yellow-stained chert particle, and Figure D-8 shows an example of a yellow-stained siltstone particle. Figure D-9 shows a carbonate coarse aggregate where the stain affected the rim in contact with the cement paste. A solution of barium chloride and potassium permanganate was used to stain sulfate-bearing minerals pink. The sulfate stain assisted with the identification of entrained air voids filled with secondary ettringite deposits observed during the ASTM C457 Modified Point Count. Figures D-10 and D-11 depict some pink-stained secondary ettringite filled air voids near a slag coarse aggregate. Note the dark coloration of the cement paste near the slag aggregate.

Table D-1. Summary of volume percentage computed from mix designs for Test Site Nos. 0, 1, 2, 3, and 4A.

Site No.	0	1	2	3	4A
Coarse Agg. Type	carbonate	blast furnace slag	natural gravel	carbonate	natural gravel
kg/m$_3$ Cement	307	285	307	285	307
kg/m$_3$ Fly Ash	46	43	46	43	46
kg/m$_3$ Water	169	162	144	157	150
kg/m$_3$ Coarse	1003	830	1211	1026	1165
kg/m$_3$ Fine	796	918	670	843	689
w/cm	0.48	0.49	0.41	0.48	0.42
Vol % Cement Paste	27.1	25.5	25.1	25.1	25.6
Vol % Coarse Agg.	37.2	34.4	43.3	37.5	42.3
Vol % Fine Agg.	29.3	33.6	25.1	30.9	25.7
Vol % Air	6.5	6.5	6.5	6.5	6.5
Cement Source	Type I Medusa	Type I Medusa	Type I Medusa	Type I Medusa	Type I Medusa
Fly Ash	Type F	Type F	Type F	Type F	Type F
Coarse Agg. No.	93-03	82-22	30-35	58-08	63-97
Fine Agg. No.	30-35	30-35	30-35	30-35	30-35

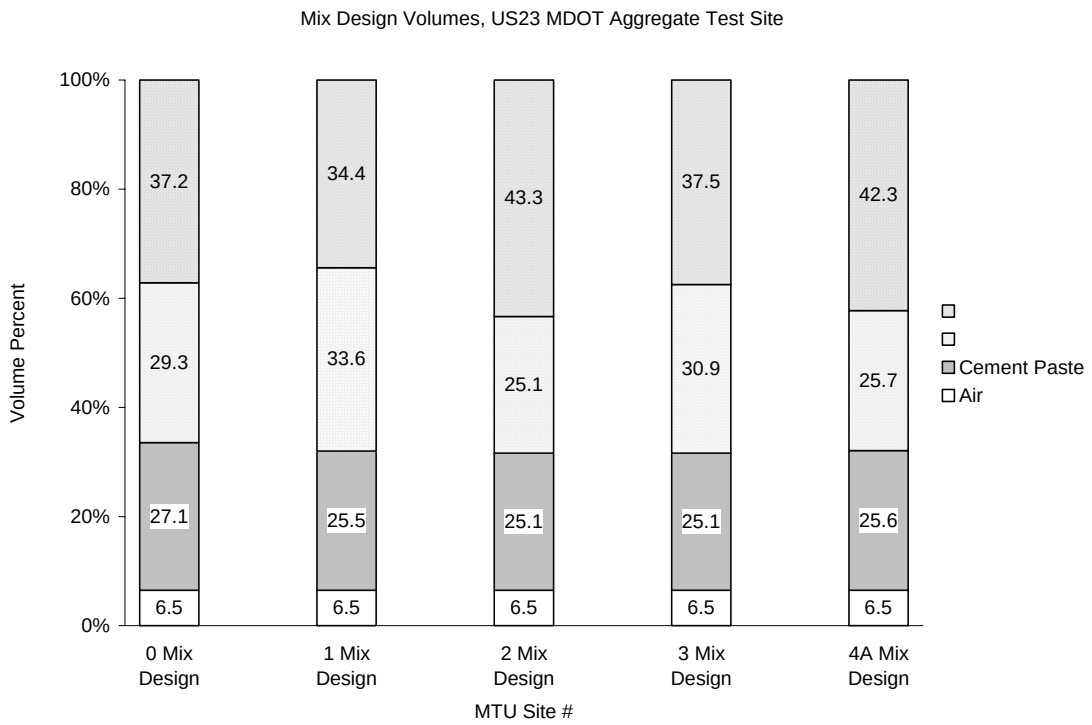

Figure D-1. Volume percentages computed from mix design information for Test Site Nos. 0, 1, 2, 3, and 4A.

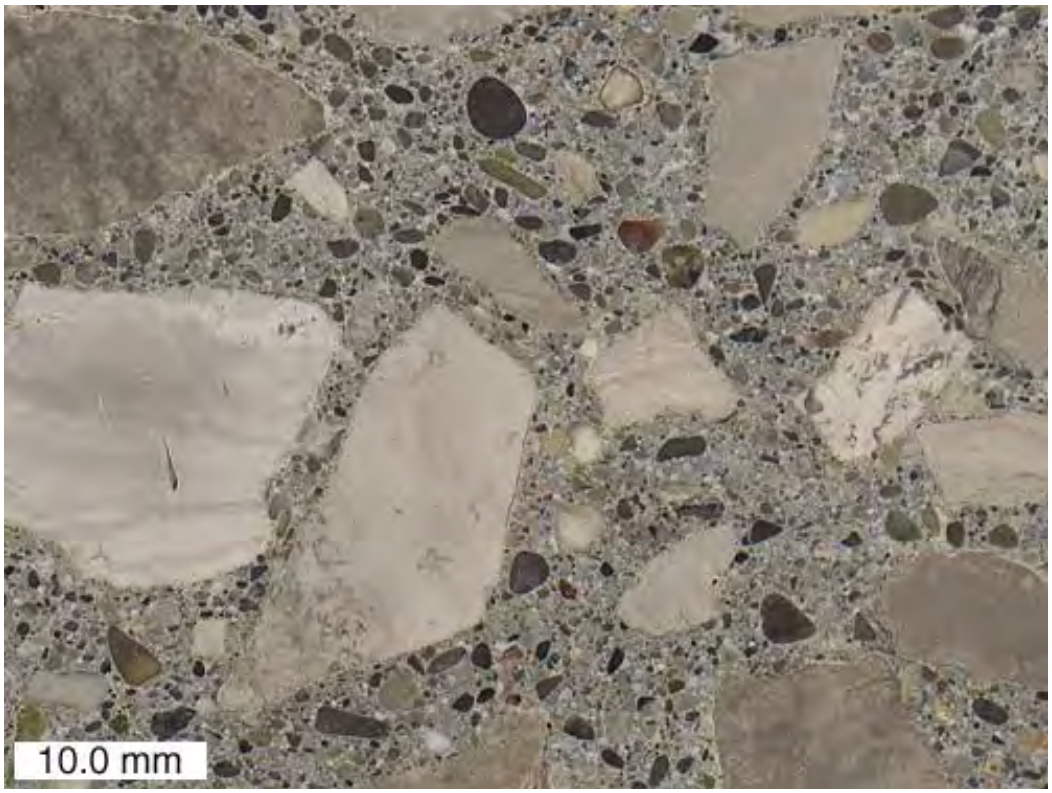

Figure D-2. View of polished surface from Core 0-A.

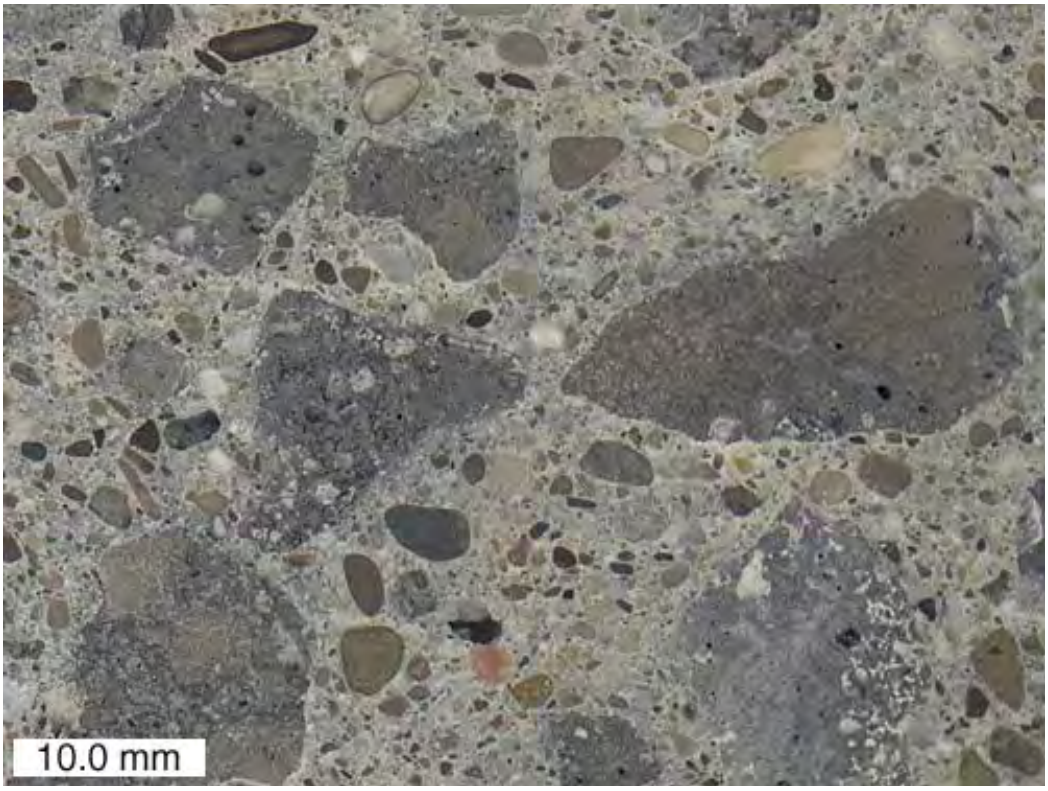

Figure D-3. View of polished surface from Core 1-A.

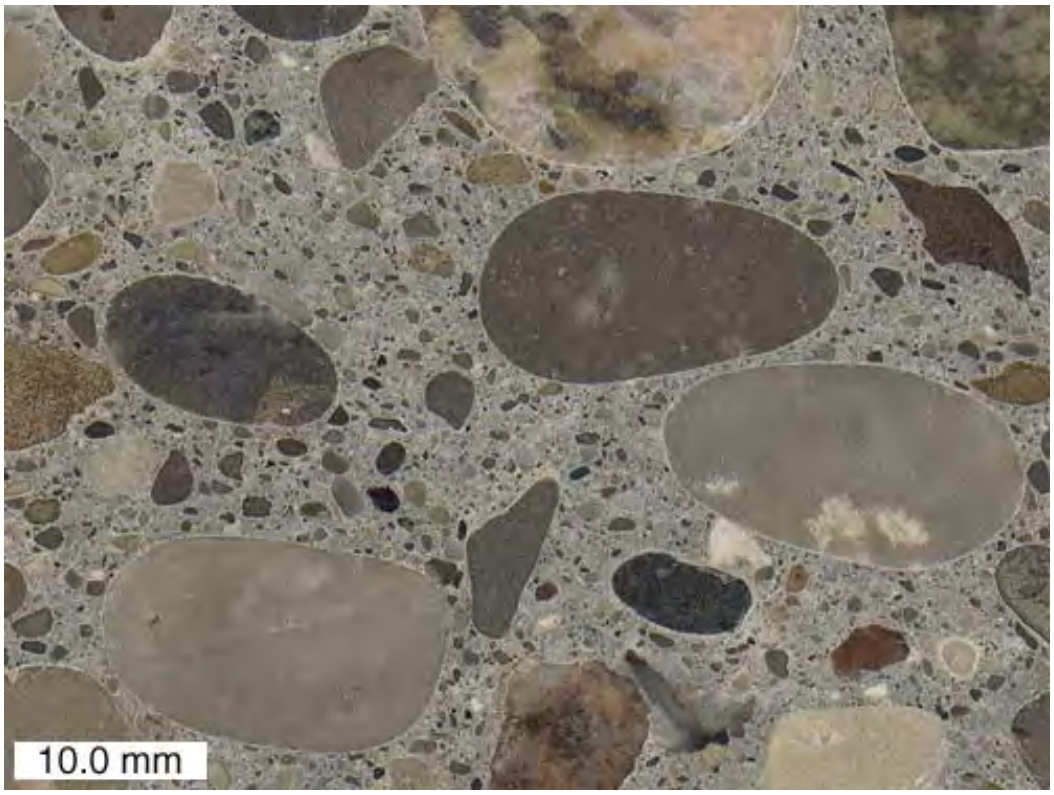

Figure D-4. View of polished surface from Core 2-A.

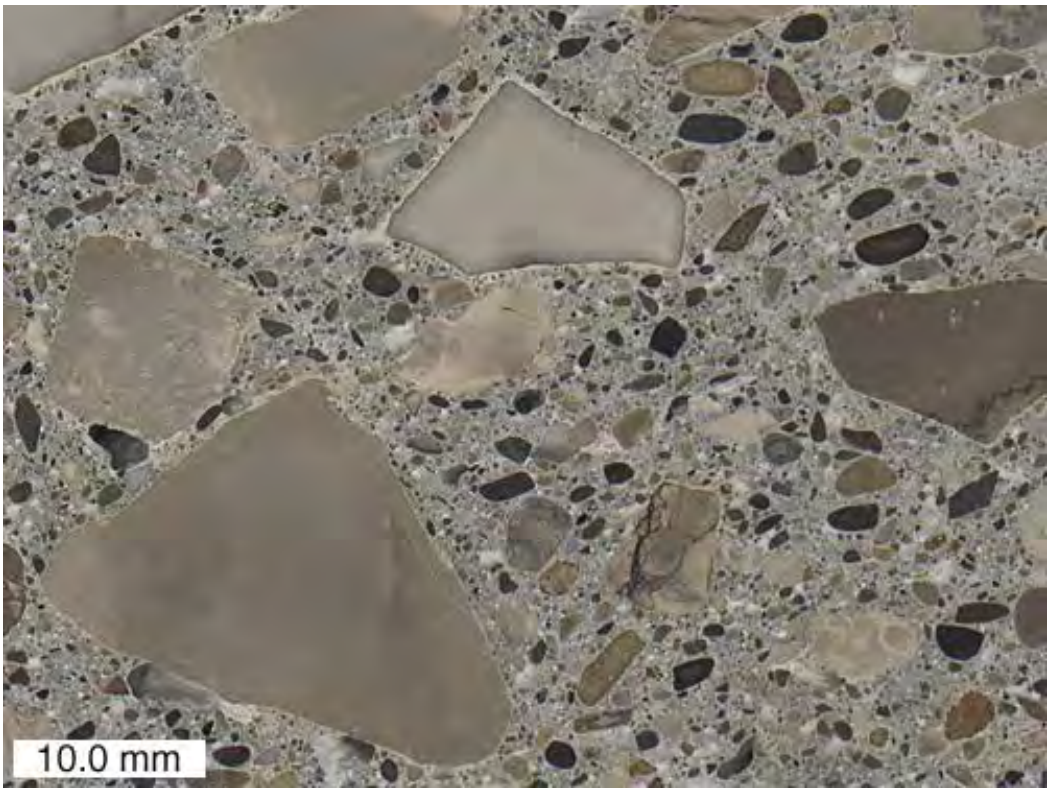

Figure D-5. View of polished surface from Core 3-A.

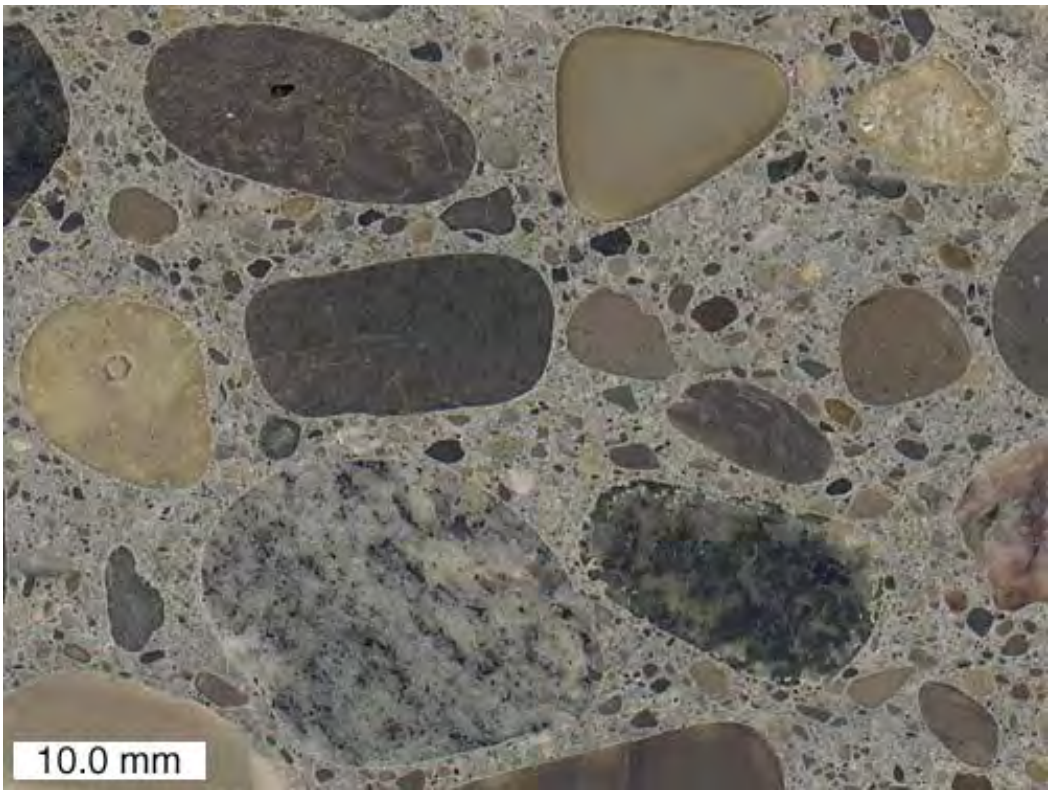

Figure D-6. View of polished surface from Core 4A-B.

Figure D-7. Yellow stained chert sand particle from Core O-A.

Figure D-8. Yellow stained siltstone sand particle from Core 3-A.

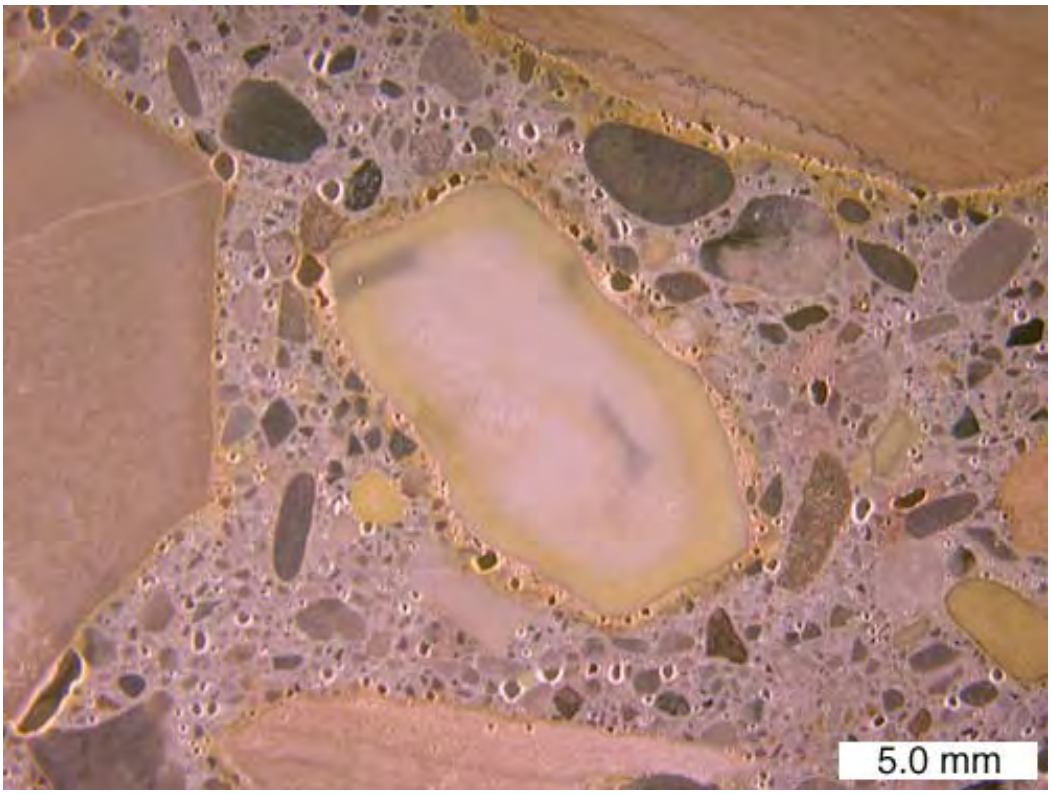

Figure D-9. Yellow stained dolomite coarse aggregate particle from Core 3-A.

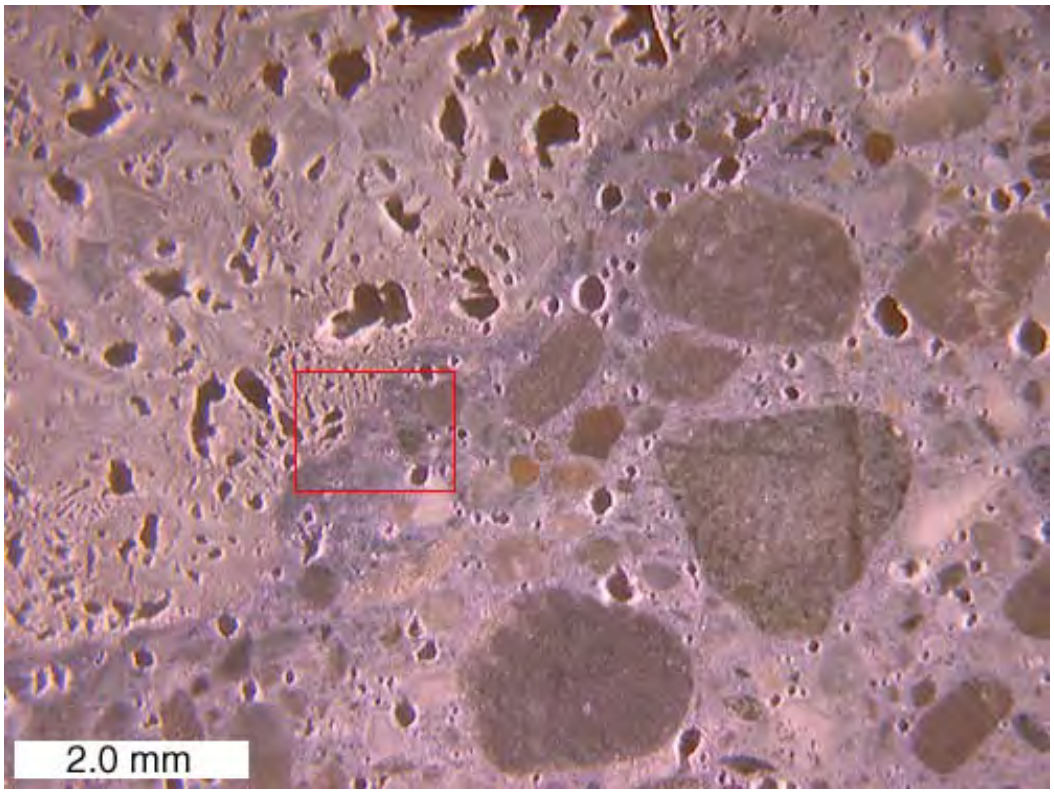

Figure D-10. A polished surface stained for sulfate minerals from Core 1-A. The red box shows the location of the close-up in Figure D-11.

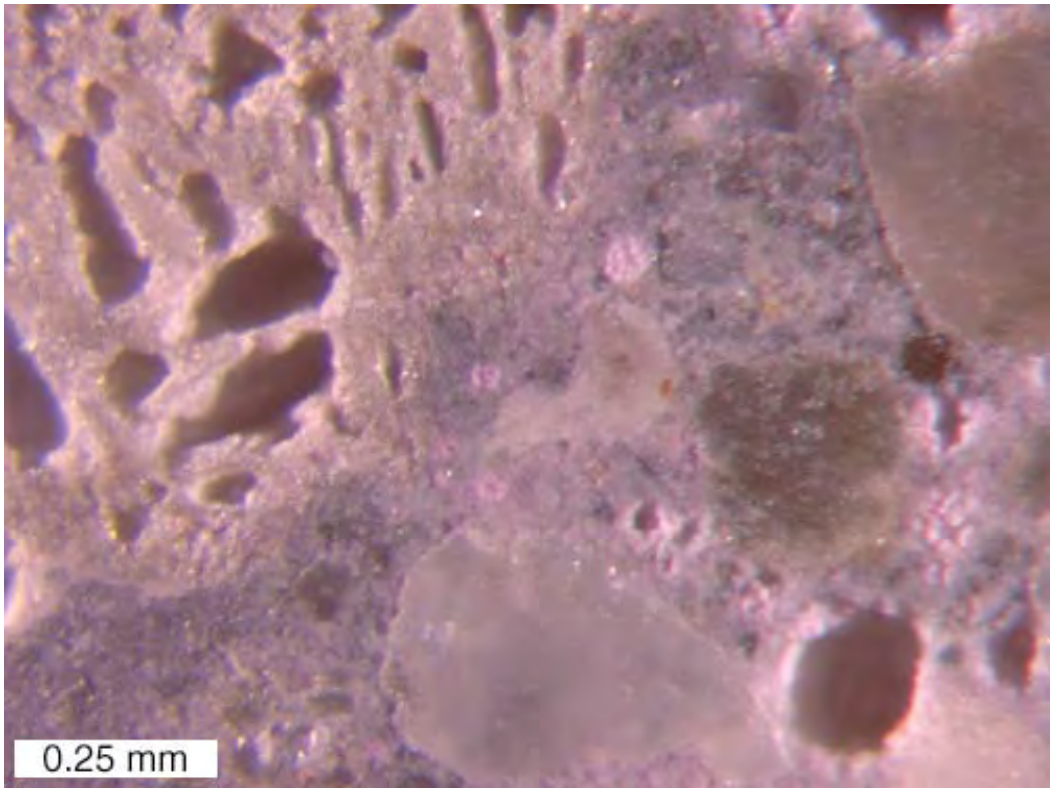

Figure D-11. Close-up of area from Figure D-10 showing ettringite filled air voids.

THIN SECTIONS

Two types of reactive fine aggregate particles were identified during the chemical staining procedures. Figures D-12a, D-12b, and D-12c show an example of a reactive chert particle. Note that there is no cracking associated with the chert. The presence of a dense rim in contact with the cement paste, and a lack of any cracking is typical of the chert particles in all five of the test sites. Figures D-13a, D-13b, and D-13c show an example of a reactive siltstone particle. Siliceous fossils within the siltstone appear to be the reactive constituent. The siltstone particle shown is cracked, but the cracks do not extend into the surrounding cement paste. The siltstone particle shown in Figures D-13a, D-13b, and D-13c is typical of the siltstone particles in all five of the pavements.

The cement paste/coarse aggregate interface was also examined in thin section. Figures D-14a, D-14b, and D-14c are an example of the interface between a carbonate coarse aggregate and the cement paste. From the cross-polarized image in Figure D-14b, it can be seen the cement paste within about 0.2 millimeters of the coarse aggregate appears carbonated. From the fluorescent image in Figure D-14c, it can be seen that the carbonated zone of cement paste is relatively porous, and that the rim of the coarse aggregate in contact with the cement paste is denser than the interior of the aggregate. Figure D-15 contains a series of elemental maps made using an SEM equipped with an EDS detector. Figures D-16a, D-16b, and D-16c are optical images of the same area. From Figure D-15, it can be seen that the carbonate aggregate contains calcium and magnesium, and is a dolomite. Also from Figure D-15, it can be seen that the cement paste in contact with the aggregate appears depleted in potassium. Furthermore, potassium bearing regions within the dolomite are associated with silicon, which suggests that the darkened rim may be due to an alkali-silica reaction where chert impurities in the dolomite have reacted with potassium from the cement paste. However, the darkened rims do not appear to be associated with any cracking or deterioration.

Figures D-17a and D-17b are an example of the interface between a slag coarse aggregate and the cement paste. From the plane-polarized image in Figure D-17a, it appears that the concentration of partially hydrated fly ash and cement particles is higher near the slag aggregate. From the fluorescent image in Figure D-17b the cement paste appears denser near the slag aggregate. Figure D-18 is a close-up view of the partially hydrated fly ash and cement near the slag aggregate. In Figure D-18, a green coloration is associated with the fly ash and the ferrite phase of the cement particles. It is suspected that the green color is due to the reduction of the iron in these materials, and is perhaps related to the calcium sulfide in the slag aggregate. Figures D-19a, D-19b, and D-19c are close-up in-situ views of the Class F fly ash particles common to the five sites. As can be seen in Figures D-19a, D-19b, and D-19c, many of the fly ash particles are composed of highly reflective opaque minerals. Figures D-20a and D-20b are close-up views of calcium sulfide dendrites in the slag coarse aggregate.

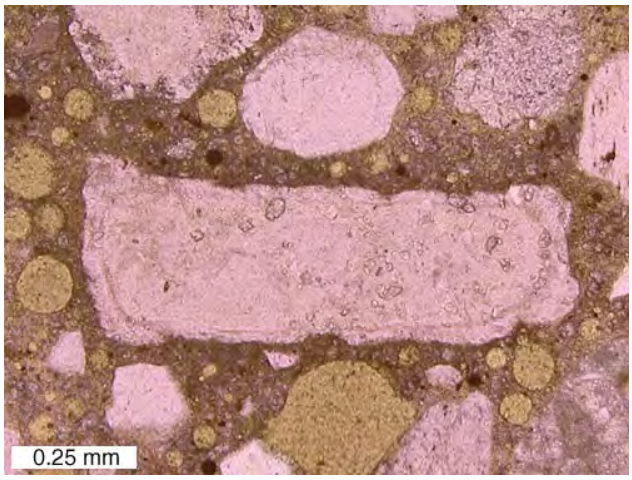

Figure D-12a. Thin-section view of a reactive chert sand particle from Core 1-A, plane-polarized light.

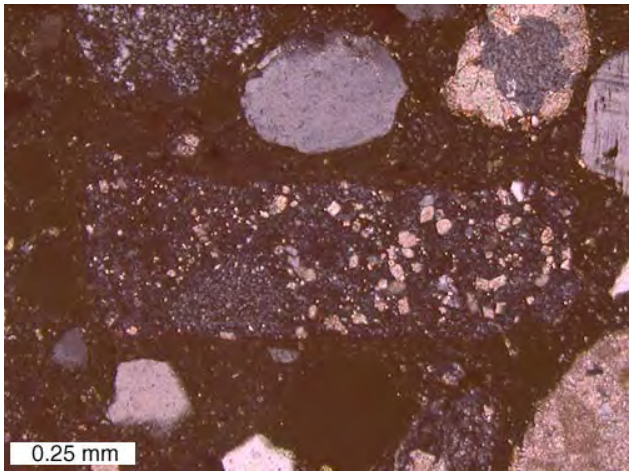

Figure D-12b. Thin-section view of a reactive chert sand particle from Core 1-A, cross-polarized light.

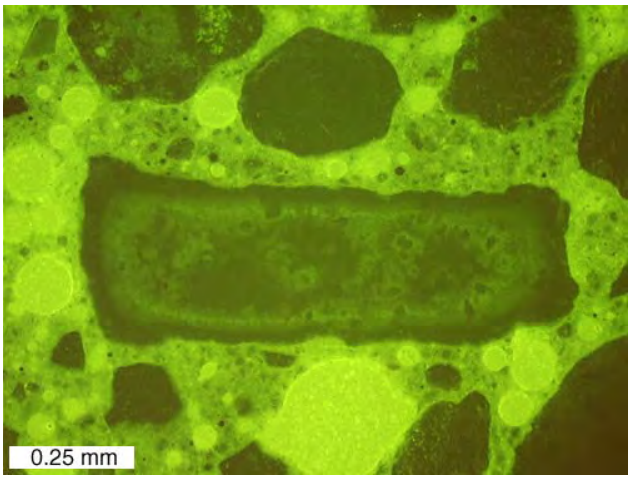

Figure D-12c. Thin-section view of a reactive chert sand particle from Core 1-A, epifluorescent mode.

Figure D-13a. Thin-section view of a reactive siltstone sand particle from Core 1-A, plane-polarized light.

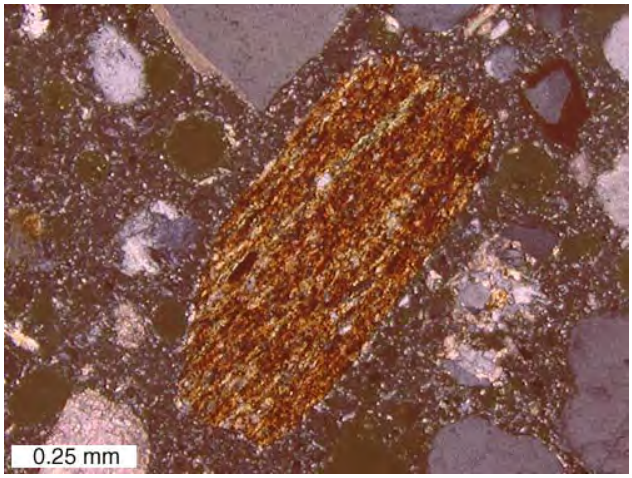

Figure D-13b. Thin-section view of a reactive siltstone sand particle from Core 1-A, cross-polarized light.

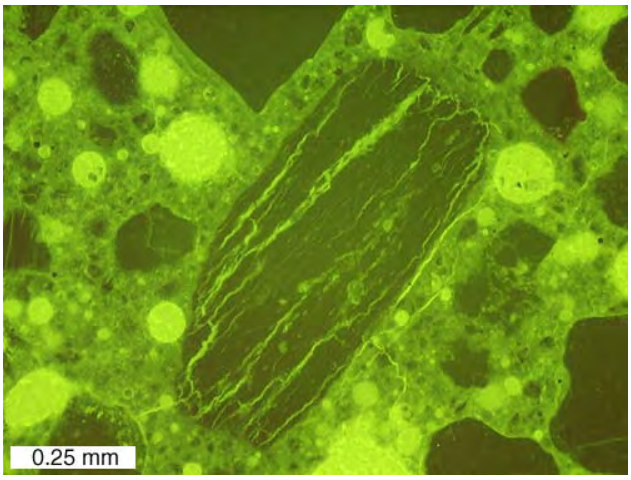

Figure D-13c. Thin-section view of a reactive siltstone sand particle from Core 1-A, epifluorescent mode.

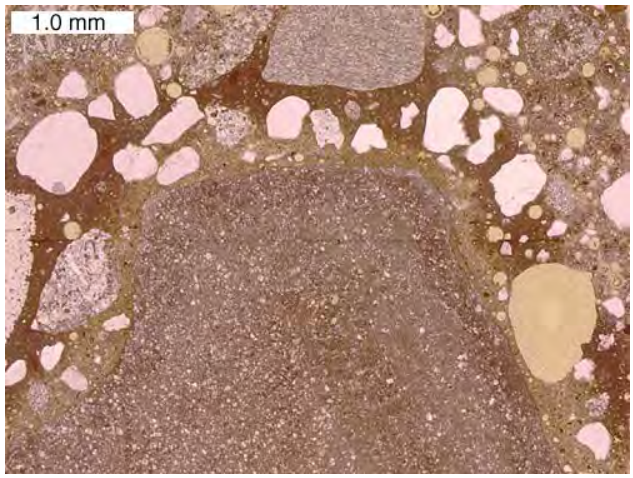

Figure D-14a. Thin-section view of a cement paste/coarse aggregate interface from Core 3-A, plane-polarized light.

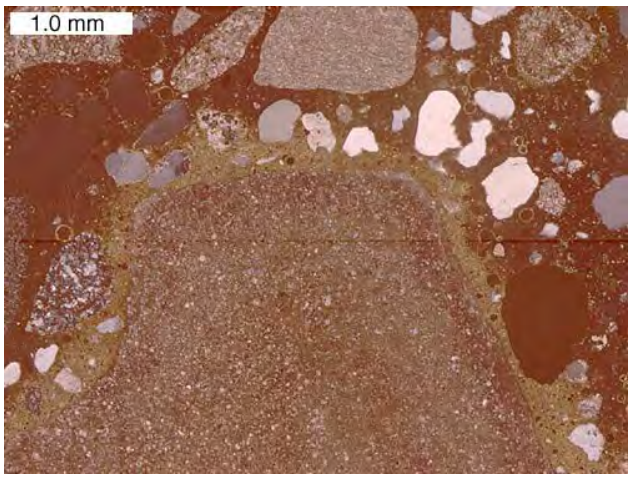

Figure D-14b. Thin-section view of a cement paste/coarse aggregate interface from Core 3-A, cross-polarized light.

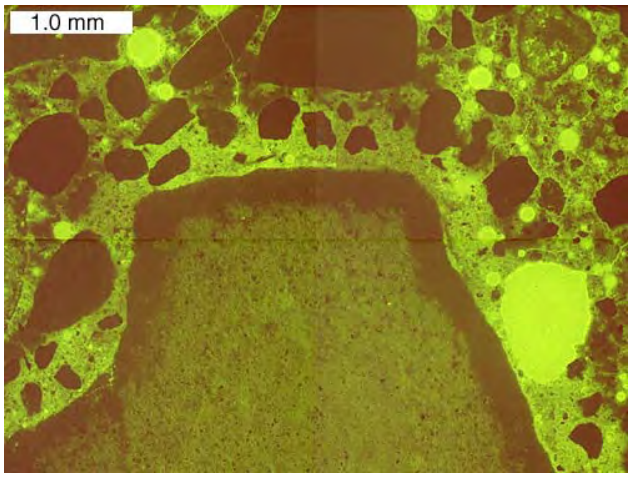

Figure D-14c. Thin-section view of a cement paste/coarse aggregate interface from Core 3-A, epifluorescent mode.

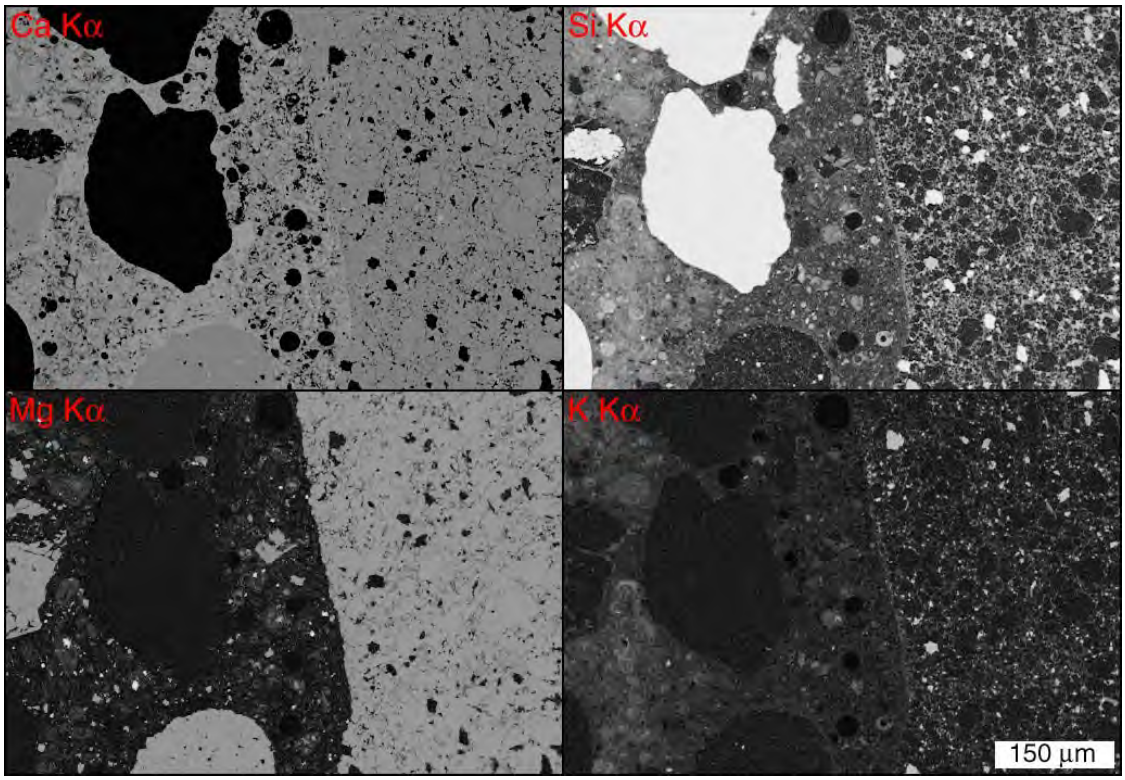

Figure D-15. Elemental maps made using an SEM equipped with an EDS detector. Brighter areas indicate a higher counts for that element.

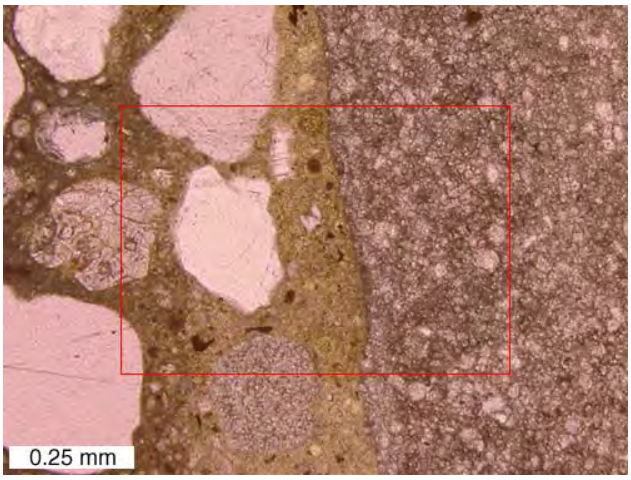

Figure D-16a. Thin-section view of a cement paste/coarse aggregate interface from Core 3-A, plane-polarized light. The red box shows the location from Figure D-15.

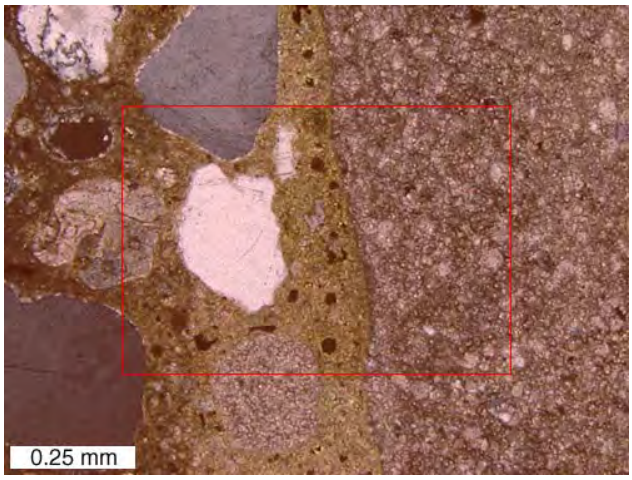

Figure D-16b. Thin-section view of a cement paste/coarse aggregate interface from Core 3-A, cross-polarized light. The red box shows the location from Figure D-15.

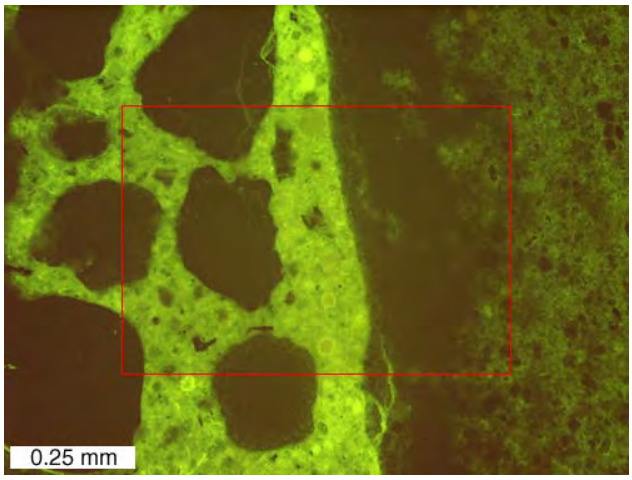

Figure D-16c. Thin-section view of a cement paste/coarse aggregate interface from Core 3-A, epifluorescent mode. The red box shows the location of the maps from Figure D-15.

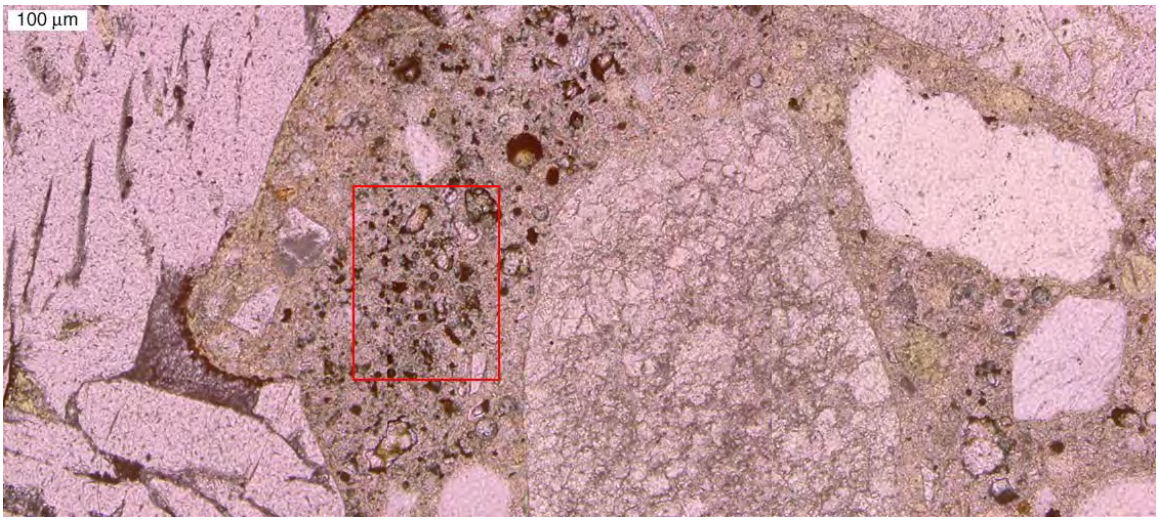

Figure D-17a. Thin-section view of a cement paste/coarse aggregate interface from Core 1-A, plane-polarized light. The red box shows the location of close-up in Figure D-18.

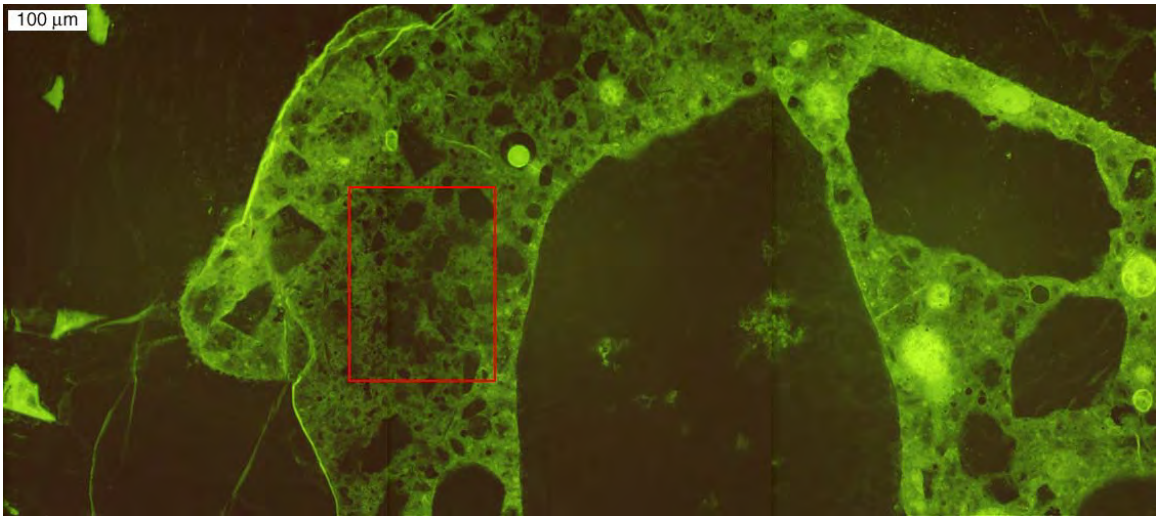

Figure D-17b. Thin-section view of a cement paste/coarse aggregate interface from Core 1-A, epifluorescent mode. The red box shows the location of close-up in Figure D-18.

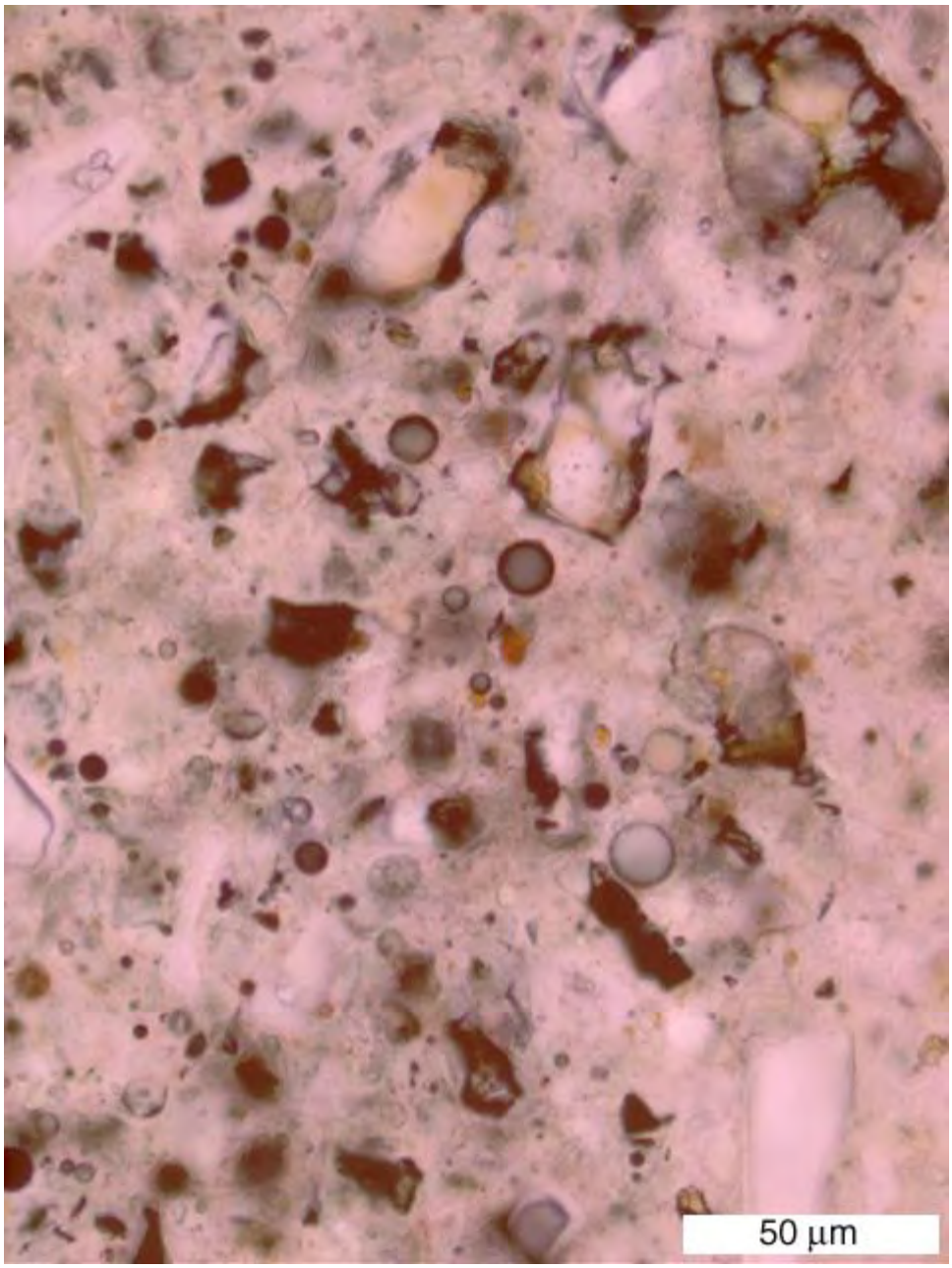

Figure D-18. Thin-section view of cement paste near contact with slag aggregate, a close-up from area outlined in red in Figures D-17a and D-17b.

Figure D-19a. Thin section view of fly ash particles from Core 0-A, combined transmitted plane-polarized light and reflected light.

Figure D-19b. Thin section view of fly ash particles from Core 0-A, combined transmitted cross-polarized light and reflected light.

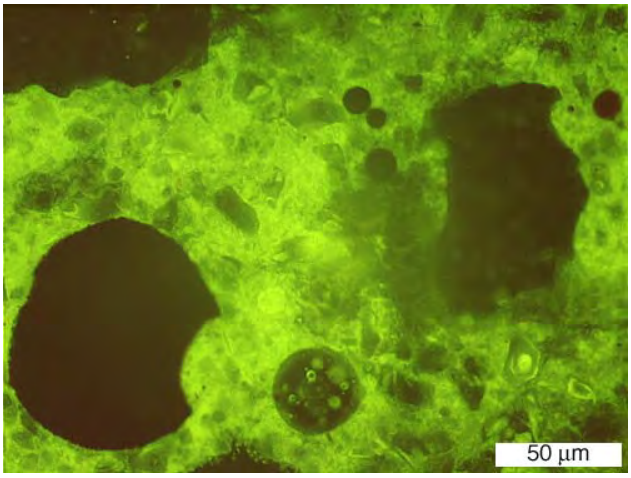

Figure D-19c. Thin section view of fly ash particles from Core 0-A, epifluorescent mode.

Figure D-20a. Thin section view of calcium sulfide dendrites in slag aggregate from Core 1-A, plane-polarized light.

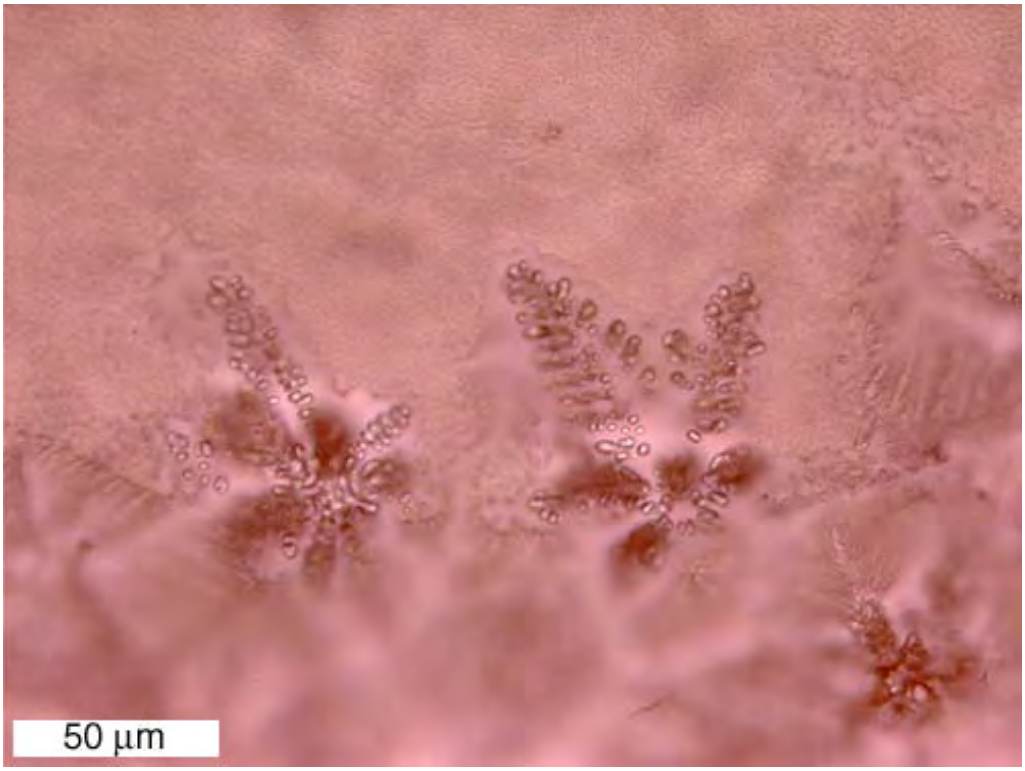

Figure D-20b. Thin section view of calcium sulfide dendrites in slag aggregate from Core 1-A, reflected light.

CHEMICAL EXTRACTIONS

A gravimetric procedure of sulfate determination was used according to British Standard 1881:Part 124. Methods for Analysis of Hardened Concrete: 1988. The weight percent SO_3 computed from the mix design assumes 3.5% by weight SO_3 for the cement and 4.5% by weight of the fly ash. The results of the sulfate determinations, expressed in terms of SO_3, are presented in Table D-2. Figure D-21 plots the computed SO_3 wt% next to the extracted SO_3 wt% for each of the sites. Neither of sites that contain natural gravel coarse aggregate have extraction values that exceed the computed value. One of the sites that contains carbonate coarse aggregate has an extraction value that exceeds the computed value, (Test Site No. 3) while the other site that contains carbonate coarse aggregate, (Test Site No. 0) does not exceed the computed value. Site 1, the only site that contains slag coarse aggregate, has an extraction value that exceeds the computed value.

A standard technique for alkali extraction from hardened concrete was not available, so an ammonium acetate extraction technique developed for the determination of exchangeable and soluble sodium and potassium in soils was adopted. The concentrations of potassium and sodium were determined by an inductively coupled plasma emission spectrophotometer. The results from the test are expressed in weight percent elemental sodium and weight percent elemental potassium. In Table D-3, the results were converted to the industry convention of kilograms of "Na_2O equivalent" per cubic meter of concrete, based on the total mass from the mix designs. The recalculation to kilograms of "Na_2O equivalent" per cubic meter of concrete allows comparisons to be made with industry standards for limiting total alkalis in the mixture. The Canadian standards specifying a maximum of 3.0 kg/m^3 Na_2O equivalent for mild protection, 2.2 kg/m^3 Na_2O equivalent for moderate protection, and 1.7 kg/m^3 Na_2O equivalent for strong protection. Figure D-22 plots the Na_2O equivalent values from extraction for all of the sites, along with dotted lines showing the Canadian protection levels.

AIR VOID CHARACTERISTICS

Slabs from each pavement were polished and examined under a stereo microscope in accordance with ASTM C457 Procedure B – Modified Point-Count Method. In addition to the standard procedure, the slabs were stained with a solution of potassium permanganate and barium chloride. The chemicals stain sulfate-bearing minerals, such as ettringite, pink. Over time, such minerals commonly occur as secondary growths in the entrained air voids. Often, entrained air voids in deteriorated concrete are completely filled with secondary ettringite. The stain assists in the identification of filled air voids that may otherwise be mistaken for hardened cement paste. In the equations used to determine the air-void system parameters, filled air voids that are identified as paste would be considered to offer no protection to freeze-thaw damage. It is controversial whether filled air voids can protect the paste against freeze-thaw damage, and thus, air-void system parameters are computed for both the concrete in its original state, and the concrete in its existing state. Table D-4 shows the results of the Modified Point-Count for the five sites. Figure D-23 plots the spacing factors for each site, along with dotted

Table D-2. Results of sulfate extractions.

MTU Core ID	Computed wt% SO_3	Extracted wt% SO_3
O-A	0.55	0.47
1-A	0.53	0.61
2-A	0.54	0.49
3-A	0.51	0.67
4A-B	0.54	0.48

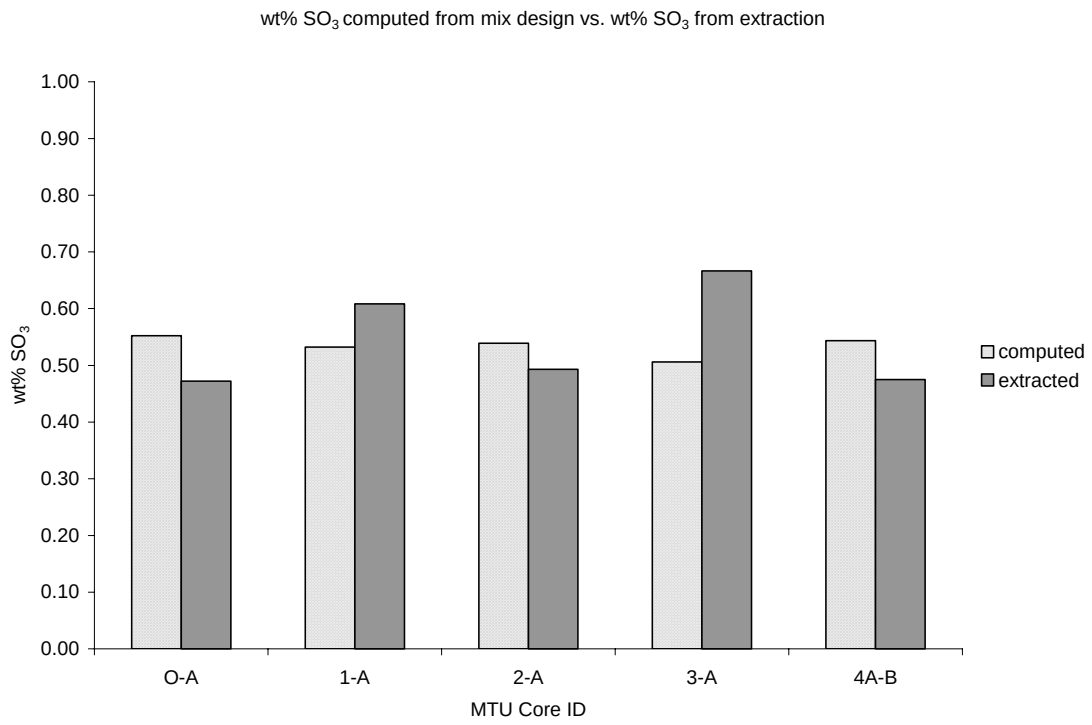

Figure D-21. Wt% SO_3 values from extraction compared to wt% SO_3 values computed from the mix design.

Table D-3. Results of alkali extractions.

MTU Core ID	Wt% Na	Wt% K	Na_2O Equivalent kg/m^3
O-A	0.021	0.036	1.29
1-A	0.026	0.038	1.46
2-A	0.021	0.038	1.35
3-A	0.021	0.033	1.27
4A-B	0.020	0.043	1.42

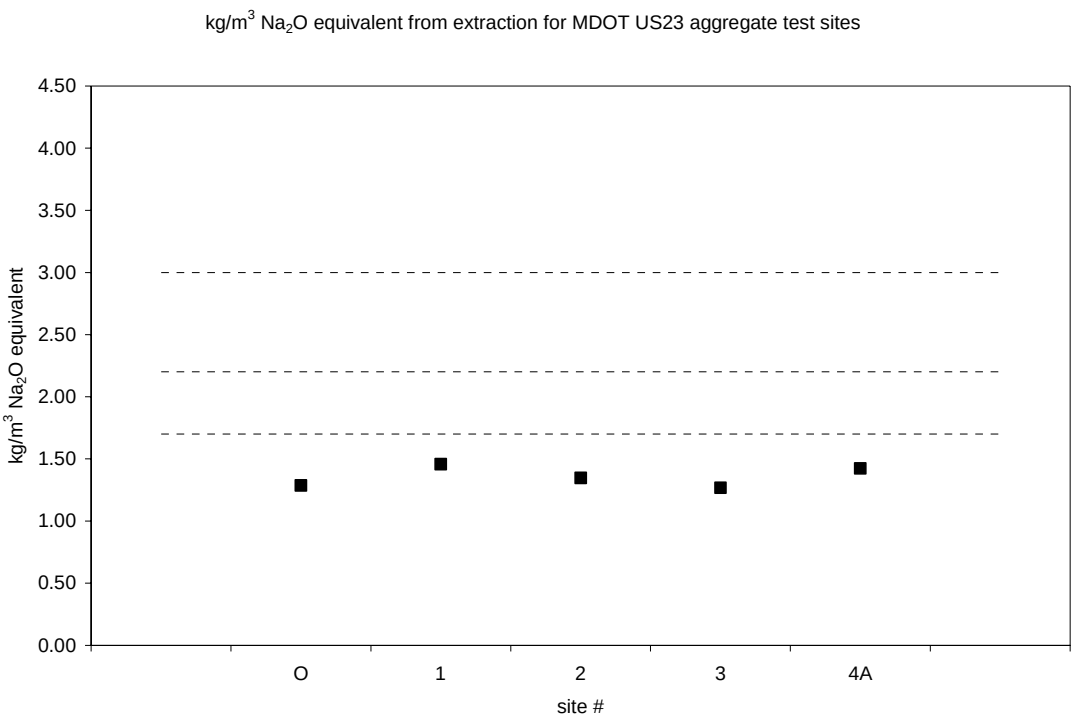

Figure D-22. Na_2O equivalent kg/m^3 values from extraction compared to Na_2O equivalent kg/m$_3$ values computed from the mix design.

Table D-4. Results of ASTM C457 Modified Point Counts.

MTU Core ID	0-C	1-A	2-C	3-C	4A-C
Raw Data					
area analyzed (cm2)	151.5	94.9	151.6	70.0	86.0
air stops	217	116	180	88	113
paste stops	732	304	734	349	264
aggregate stops	2006	921	2044	929	1055
secondary ettringite stops	5	9	4	2	1
total stops	2960	1350	2962	1368	1433
traverse length (mm)	7732	4134	7737	3573	4054
# of air void intercepts	3728	1275	2376	892	1626
# of secondary ettringite filled intercepts	207	170	288	80	5
Results					
vol% aggregate	67.8	68.2	69.0	67.9	73.6
vol% air original	7.5	9.3	6.2	6.6	8.0
vol% air existing	7.3	8.6	6.1	6.4	7.9
vol% paste original	24.7	22.5	24.8	25.5	18.4
vol% paste existing	24.9	23.2	24.9	25.7	18.5
original void frequency (voids/m)	509	350	344	272	402
existing void frequency (voids/m)	482	308	307	250	401
original avg. chord length (mm)	0.147	0.265	0.180	0.242	0.198
existing avg. chord length (mm)	0.152	0.279	0.198	0.258	0.197
original specific surface (mm^{-1})	27.1	15.1	22.2	16.5	20.2
existing specific surface (mm^{-1})	26.3	14.4	20.2	15.5	20.3
original paste/air ratio	3.3	2.4	4.0	3.9	2.3
existing paste/air ratio	3.4	2.7	4.1	4.0	2.3
original spacing factor (mm)	0.121	0.161	0.180	0.234	0.114
existing spacing factor (mm)	0.129	0.188	0.203	0.257	0.115

lines to represent the suggested range according to ASTM C457. Figure D-24 plots the void frequency for each site, along with dotted lines to represent the suggested range according to ASTM C457. Figure D-25 compares the aggregate, cement paste and air volume percentages as determined by point count to the volume percentages computed from the mix design.

CONCLUSIONS

The results of the evaluation of the cores received from the MDOT US-23 Aggregate Test Site are from pavements constructed in the years 1993 and 1994. The cores, representing five different coarse aggregate types (two carbonate sources, two natural gravel sources, and one blast furnace slag source), are all from pavements in good condition. As would be assumed, differences in the microstructure exist in the concrete from the various test sites, primarily as a result of the coarse aggregate. These differences can be summarized as follows:

- In Test Site No. 3, the rims where the dolomite aggregates (Pit No. 58-08) contacted the paste stained positively for alkali-silica reaction product, a finding that is confirmed by petrographic analysis. Further, this reaction is associated with increased porosity and carbonation of the surrounding cement paste and densification of the aggregate rims. It seems that the darkened rims are due to an alkali-silica reaction where chert impurities in the dolomite have reacted with potassium from the cement paste. However, the darkened rims do not appear to be associated with any cracking or deterioration.
- It appears that the concentration of partially hydrated fly ash and cement particles is higher near the slag aggregate than in the bulk paste, with a corresponding increase in paste density. In addition, a green coloration is associated with the fly ash and the ferrite phase of the cement particles. It is suspected that the green color is due to the reduction of the iron in these materials, and is perhaps related to the calcium sulfide in the slag aggregate.
- The results of the sulfate extraction found that the measured sulfate content was lower than the predicted in 3 of the 4 mixtures containing natural aggregates. In the case of mixtures made with the slag (Pit No. 82-22) and the dolomite (Pit No. 58-08) coarse aggregate, the measured sulfate contents were higher then predicted. This finding, which was confirmed through repeating the test, suggests that slag and some natural aggregates may provide a source of internal sulfate.

In addition to differences observed between the mixtures due to the coarse aggregate type, the following observations were made:

- Two types of reactive fine aggregate particles were identified during the chemical staining procedures and petrographic analysis. One type is reactive chert that stained yellow after treatment with sodium cobaltinitrite and developed dense rims in contact with the cement paste. There was no cracking associated with the chert particles in any of the five of the test sites. The second reactive fine aggregate particle is a reactive siltstone that contains siliceous fossils that appear to be the reactive

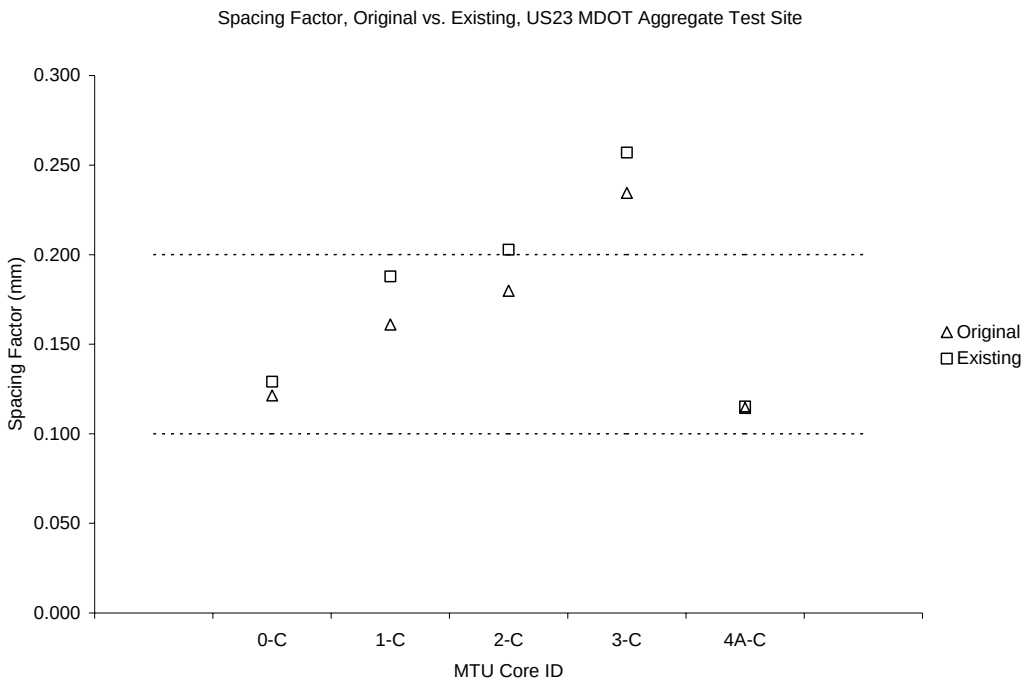

Figure D-23. Spacing factors plotted with dotted lines showing suggested values from ASTM C457.

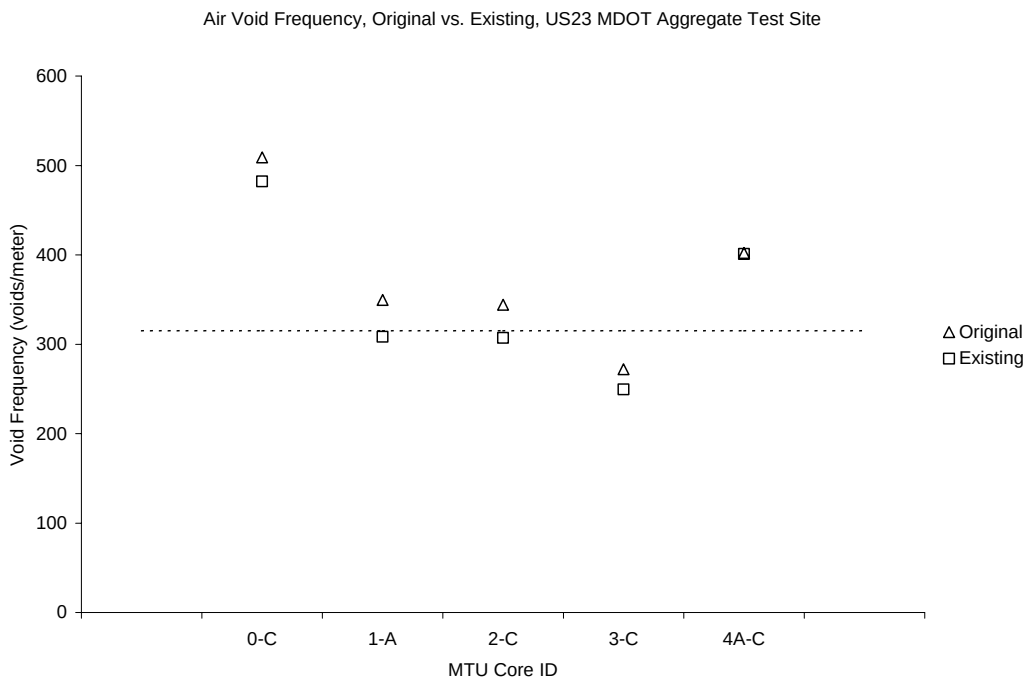

Figure D-24. Void frequencies plotted with dotted lines showing suggested values from ASTM C457.

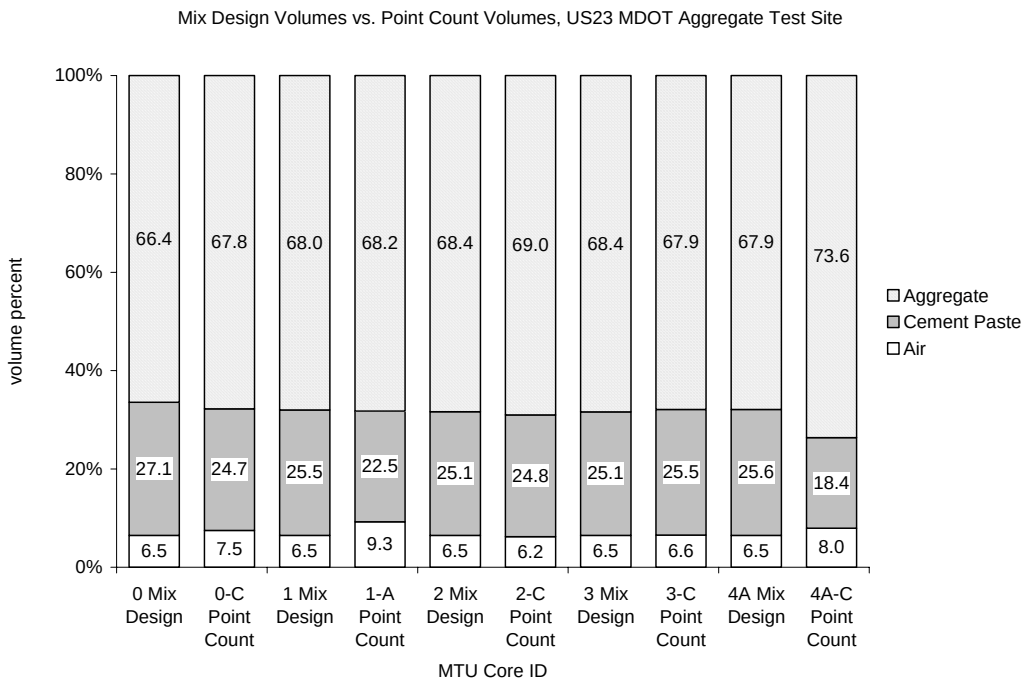

Figure D-25. Volume percentages from point counts compared to volume percentages computed from mix designs.

constituent. Typically, the siltstone particles are cracked, but the cracks do not extend into the surrounding cement paste. This is typical of the siltstone particles in all five of the pavements.

- The Class F fly ash, which is largely composed of highly reflective opaque minerals, is common to all five sites. It is interesting to note that in the presence of this fly ash, that none of the potential ASR was deleterious and that the higher than expected sulfate levels in two of the sites had no apparent ill effect. Also, the overall alkali levels in the mixtures were well below that needed to protect the concrete against ASR.

SITES 26A, 26B, AND 27: THE MDOT US10 CLARE TEST SITE

INTRODUCTION

The cores received from the MDOT US10 Clare Test Site are from pavements in poor condition. The three sites all have the same mix design, which is shown in Table D-5. However, the subbase materials used at the sites were not the same. Both Test Sites Nos. 26A and 26B utilized an asphalt treated permeable base, while Test Site No. 27 was supported on an aggregate base. To investigate the sites, slabs were cut from the cores in a plane perpendicular to the pavement surface. Some of the slabs were polished and used for chemical staining and stereo OM, other slabs were cut into billets and prepared in thin section.

CHEMICAL STAINING

A solution of sodium cobaltinitrite was applied to the polished slab surfaces to stain potassium-bearing alkali-silica gels yellow. A variety of aggregate types picked up the yellow stain, including cherts, impure cherty carbonates, and sandstones. Figures D-26 through D-28 depict some cracked coarse aggregates where alkali-silica reaction product in the cracks has picked up the yellow stain. A solution of barium chloride and potassium permanganate was used to stain sulfate-bearing minerals pink. The sulfate stain assisted with the identification of entrained air voids filled with secondary ettringite deposits observed during the ASTM C457 Modified Point Count. Figure D-29 depicts some pink-stained secondary ettringite filled air voids from core 27-B.

THIN SECTIONS

Figures D-30a, D-30b, and D-30c show some cracked coarse aggregates from core 26B-C. Figures D-31a, D-31b, and D-31c are a close-up view of the alkali-silica reaction product that fills the crack. Measurements of the capillary porosity of the cement paste from the three sites were made using fluorescence microscopy. To make the measurements, thin sections were made from cores 26A-C, 26B-C, and 27-C at representative depths of 5 cm, 10 cm, and 15 cm from the pavement surface. From each thin section, six regions of cement paste and fine aggregate were sampled, for a total of 18 images for each site. Each image consists of the 8-bit G band from the complete 24-bit RGB image originally captured from the microscope. Figures D-32, D-33, and D-34 consist of a composite image showing all of the images used from each site. In the figures, the dark areas are fine aggregate particles, the bright areas are entrained air bubbles, and the intermediately bright areas are the cement paste. Figure D-35 shows the summary brightness histogram for the three sites. For each site, the histogram shows three distinct peaks: a large peak in the dark region for the fine aggregates, a broad peak in the middle for the cement paste, and a small peak in the bright region for the entrained air bubbles. From Figure D-35, it appears that the cement paste from core 26A-C is slightly more dense (darker) than the cement paste from the other two cores, 26B-C, and 27-C. One explanation for this observation is that the *w/cm* for Test Site 26A was lower than for the other two test sites.

Table D-5. Mix design information for Test Site Nos. 26A, 26B, and 27.

Site No.	26A, 26B, and 27
kg/m^3 Cement	252
kg/m^3 Fly Ash	0
kg/m^3 Water	121
kg/m^3 Coarse	1158
kg/m^3 fine	629
w/cm	0.48
Vol% Cement Paste	21.3
Vol% Coarse Agg.	46.5
Vol% Fine Agg.	25.7
Vol% Air	6.5
Coarse Agg. No.	67-02
Fine Agg. No.	67-02

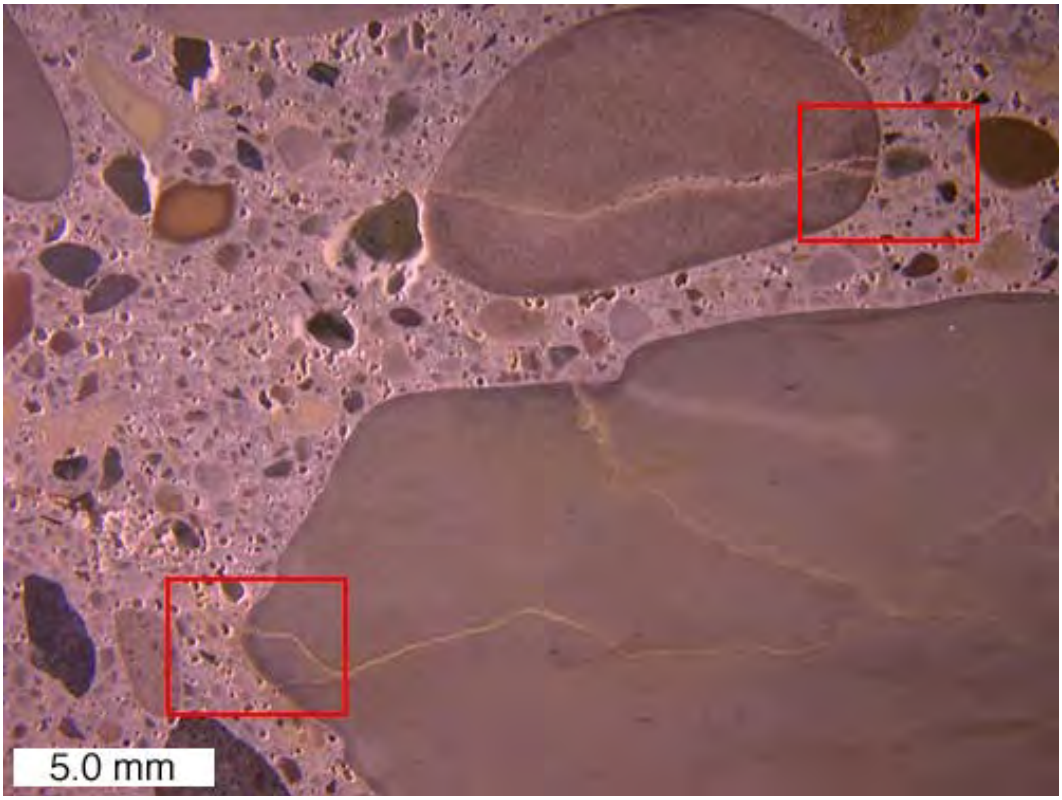

Figure D-26. Cracked coarse aggregates where alkali-silica gel product in the cracks has picked up the yellow sodium cobaltinitrite stain in Core 27-B. Red boxes show close-up areas depicted in Figures D-27 and D-28.

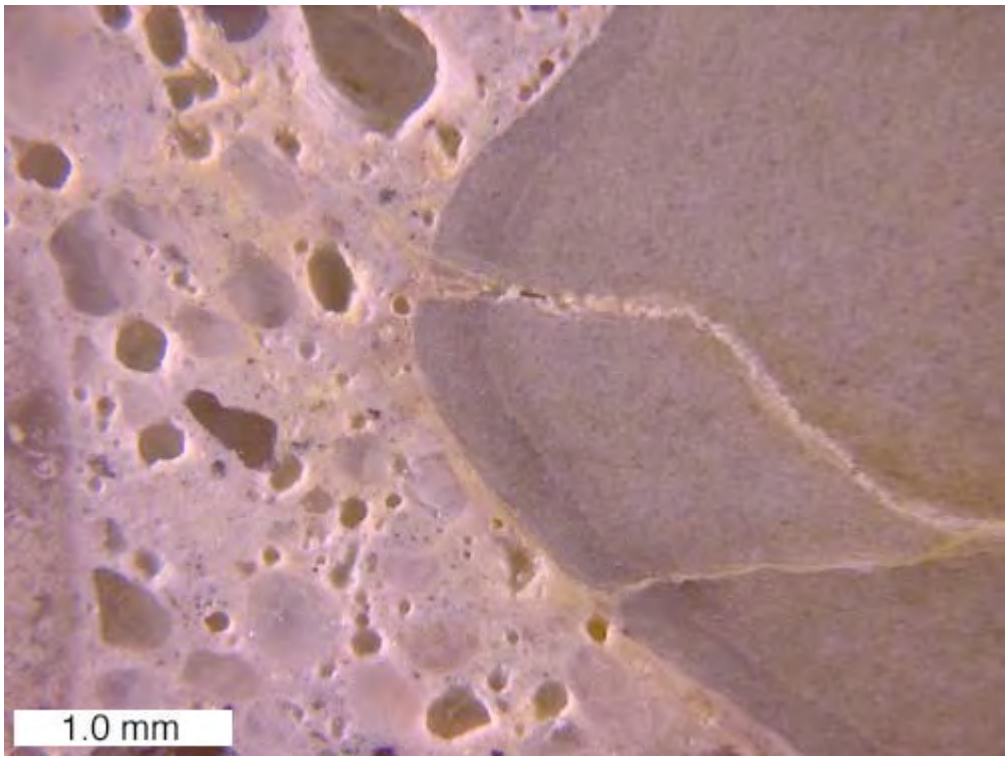

Figure D-27. Alkali-silica reaction product in cracks that has picked up the yellow sodium cobaltinitrite stain, close-up of area outlined in red in Figure D-26.

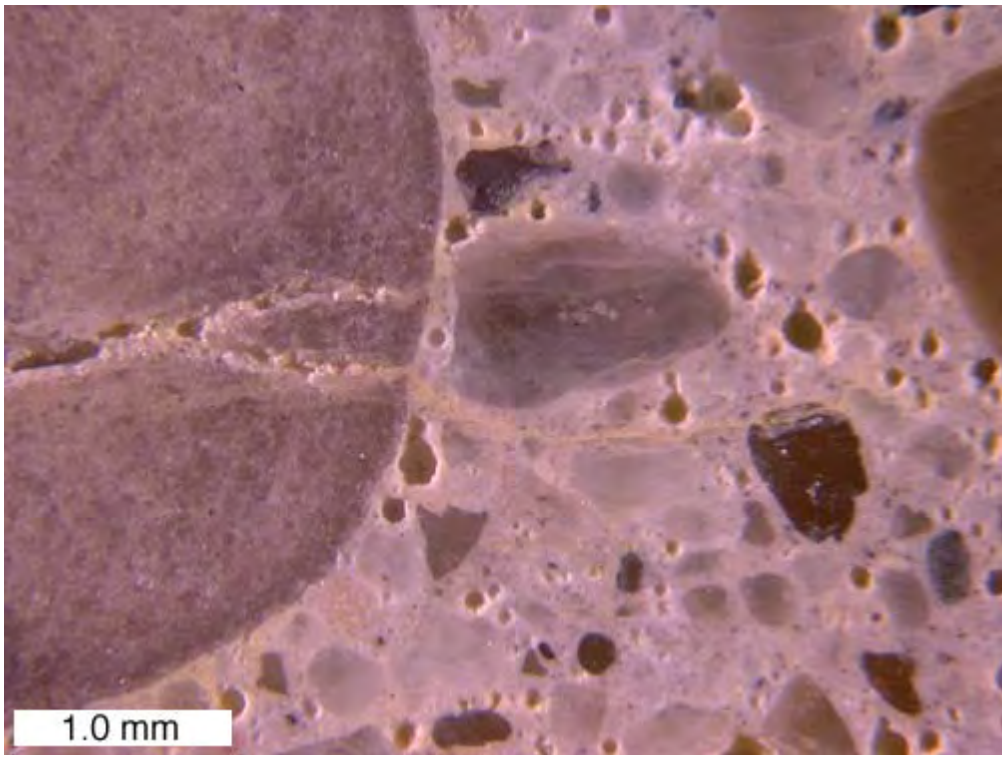

Figure D-28. Alkali-silica reaction product in cracks that has picked up the yellow sodium cobaltinitrite stain, close-up of area outlined in red in Figure D-26.

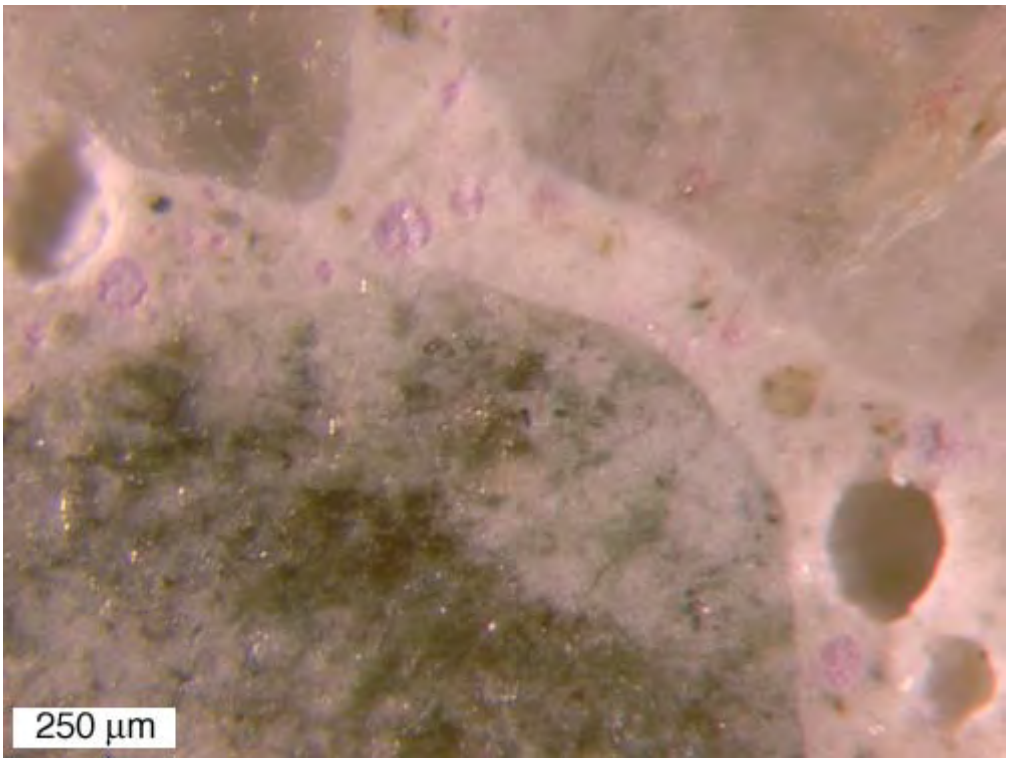

Figure D-29. Ettringite filled entrained air voids stained pink from core 27-B.

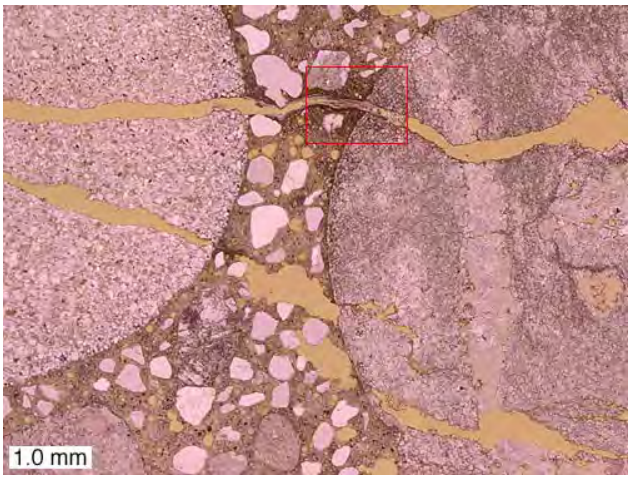

Figure D-30a. Thin-section view of cracked coarse aggregates from Core 26B-C, plane-polarized light. Red box shows area of close-up view in Figure D-31a.

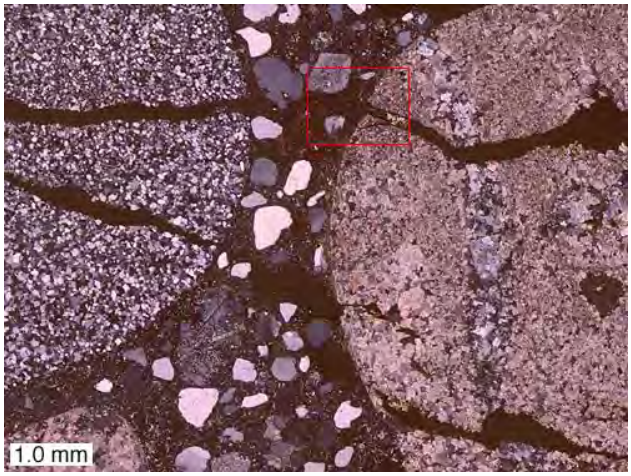

Figure D-30b. Thin-section view of cracked coarse aggregates from Core 26B-C, cross-polarized light. Red box shows area of close-up view in Figure D-31b.

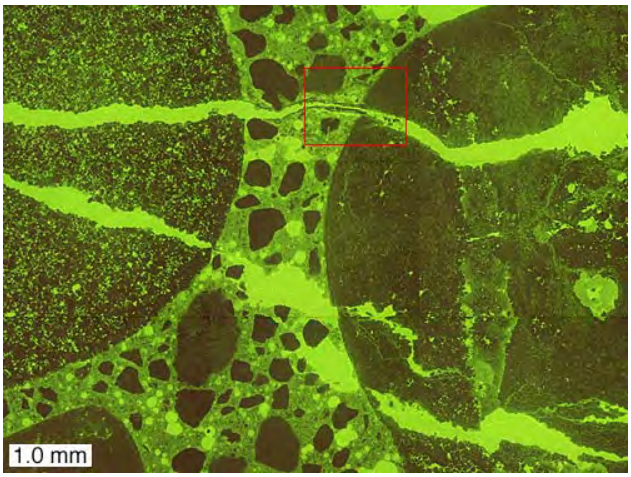

Figure D-30c. Thin-section view of cracked coarse aggregates from Core 26B-C, epifluorescent mode. Red box shows area of close-up view in Figure D-31c.

Figure D-31a. Thin section view of alkali-silica reaction product in crack, plane-polarized light, close-up of area outlined in red in Figure D-30a.

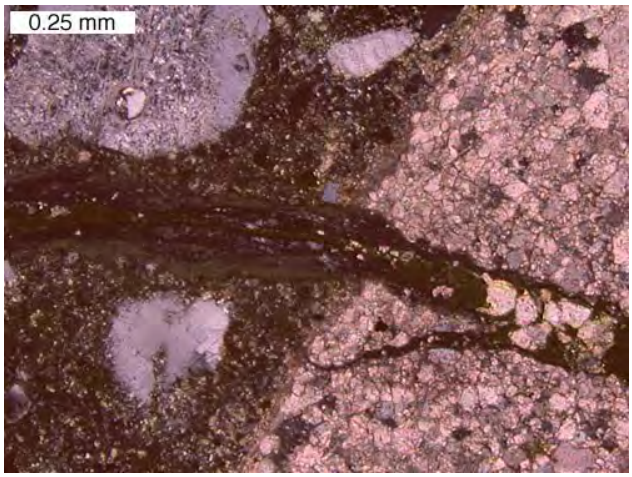

Figure D-31b. Thin section view of alkali-silica reaction product in crack, cross-polarized light, close-up of area outlined in red in Figure D-30b.

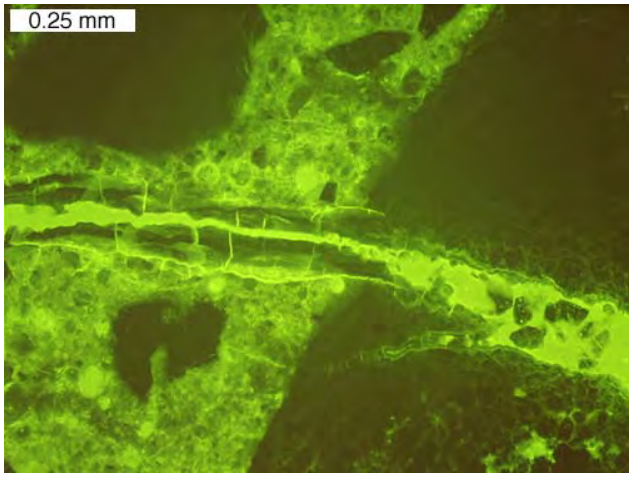

Figure D-31c. Thin section view of alkali-silica reaction product in crack, epifluorescent mode, close-up of area outlined in red in Figure D-30c.

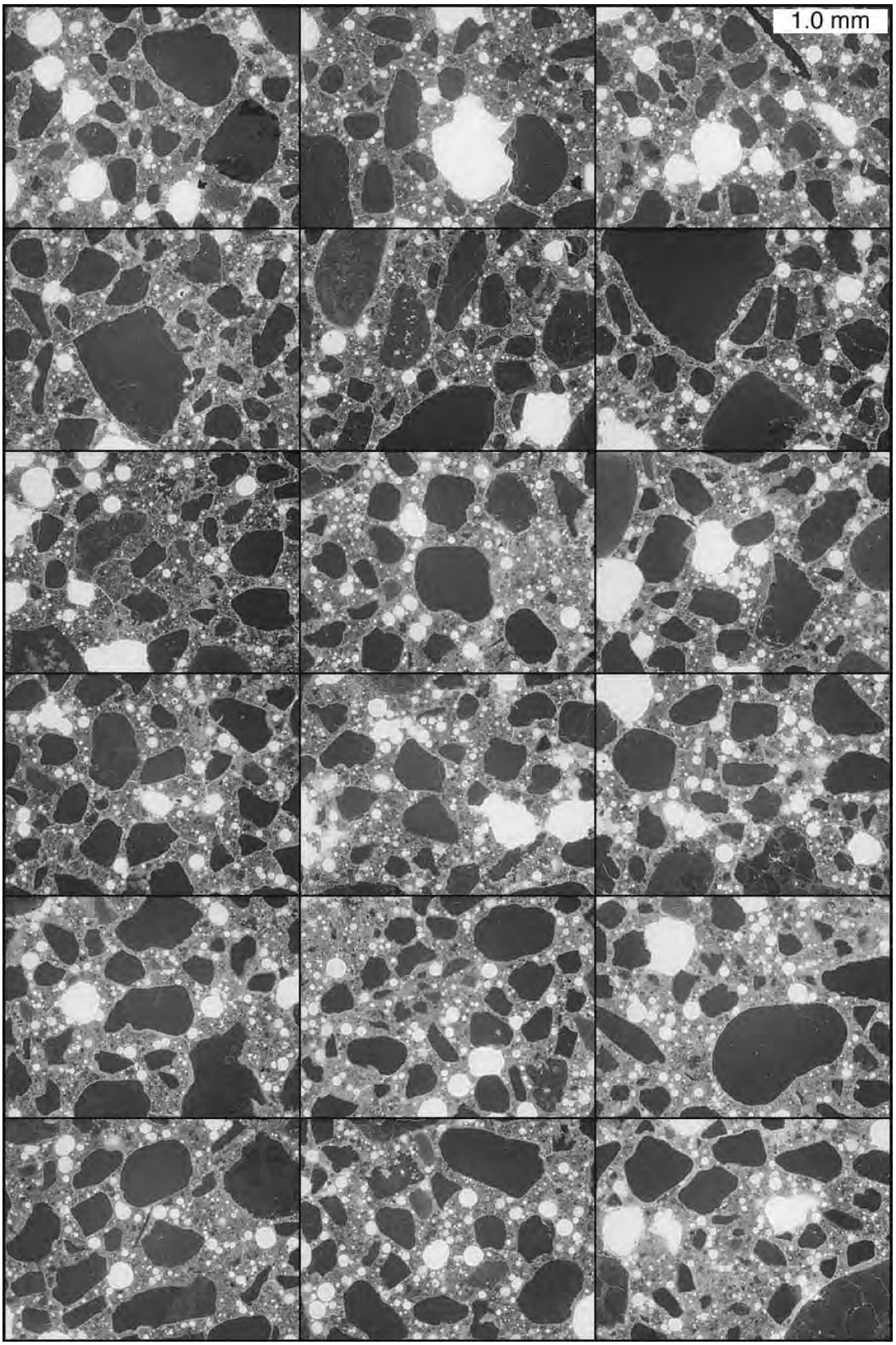

Figure D-32. Composite of 18 epifluorescent mode images used to measure cement paste capillary porosity in Core 26A-C.

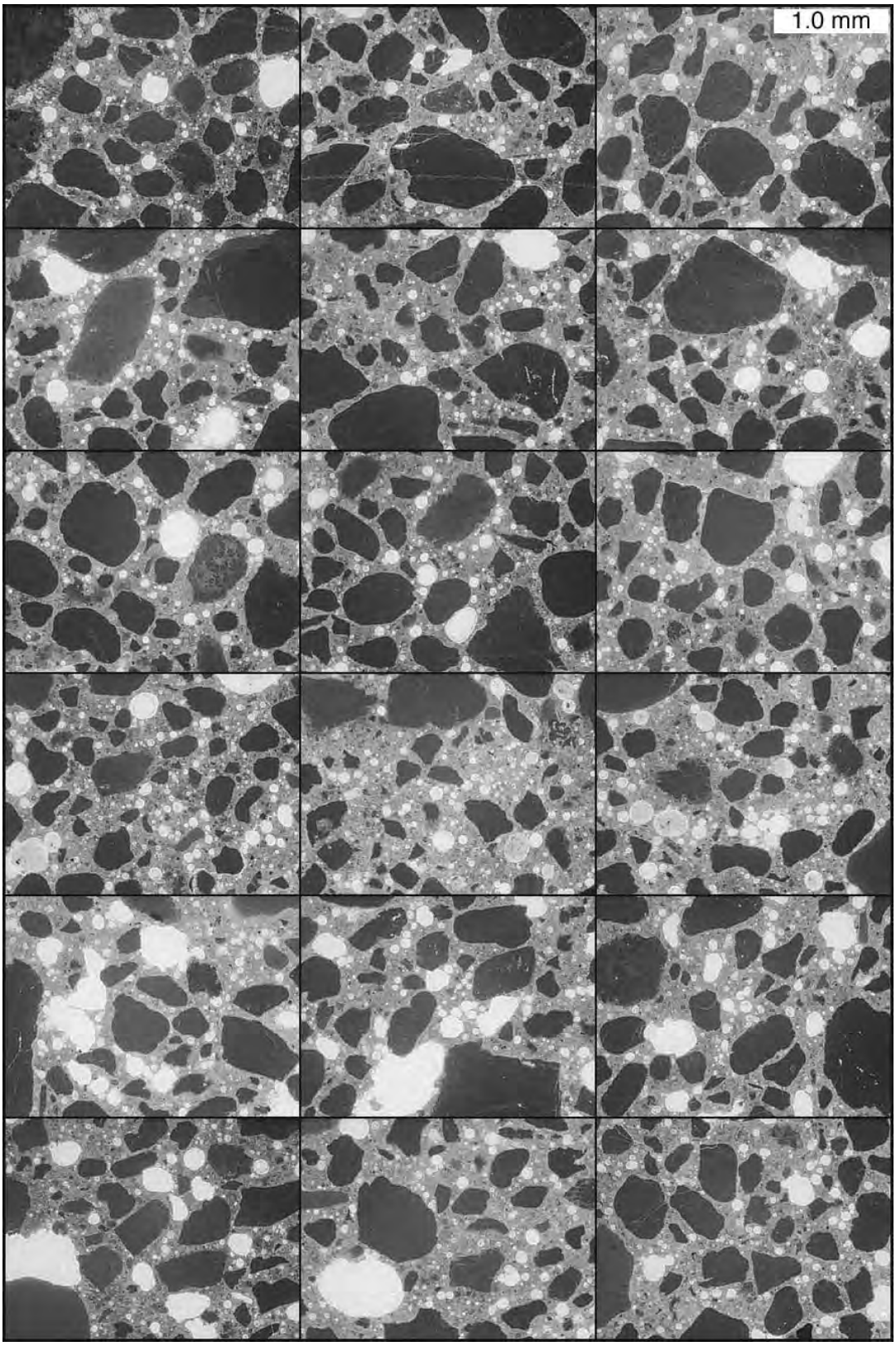

Figure D-33. Composite of 18 epifluorescent mode images used to measure cement paste capillary porosity in Core 26B-C.

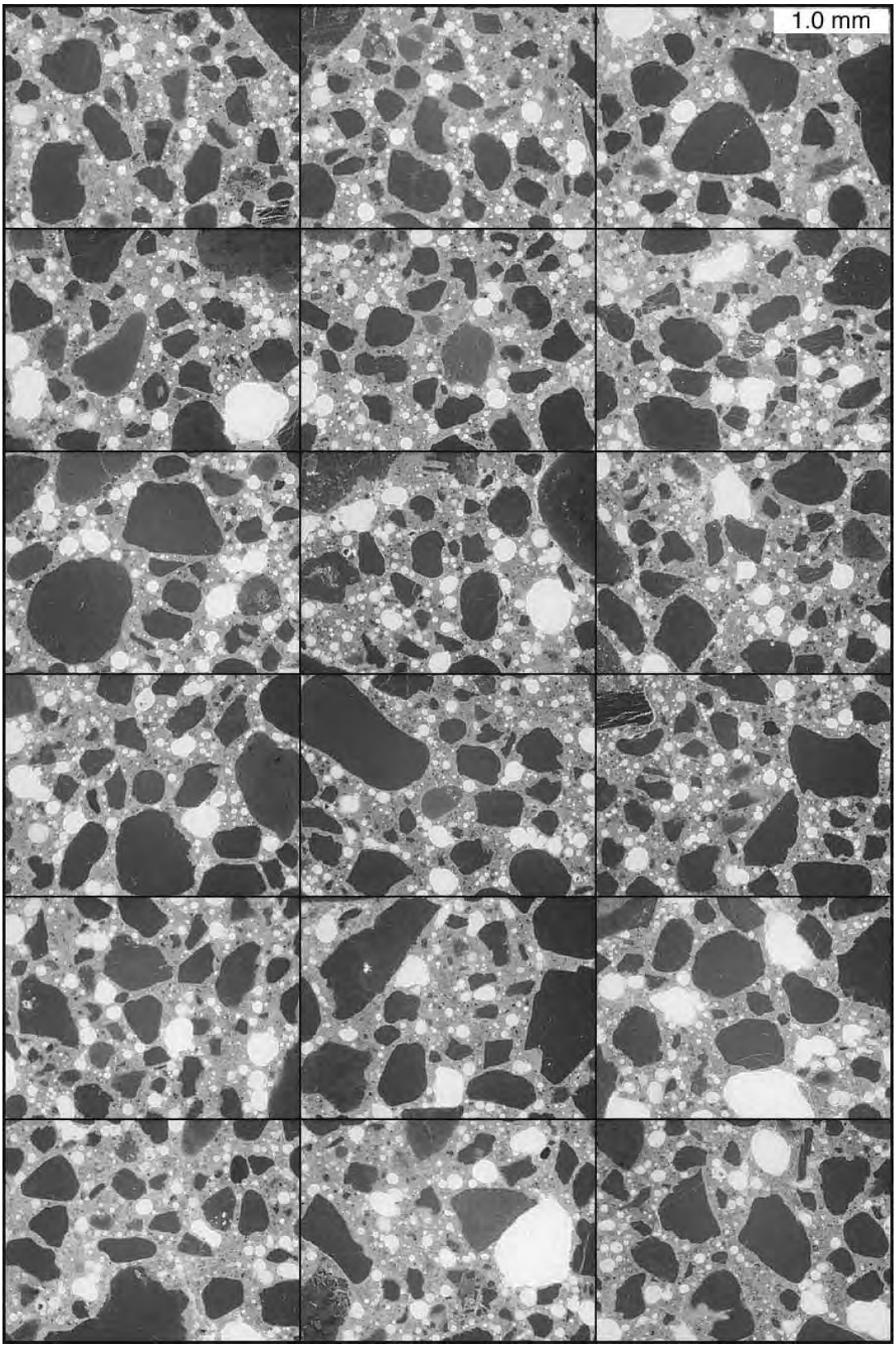

Figure D-34. Composite of 18 epifluorescent mode images used to measure cement paste capillary porosity in Core 27-C.

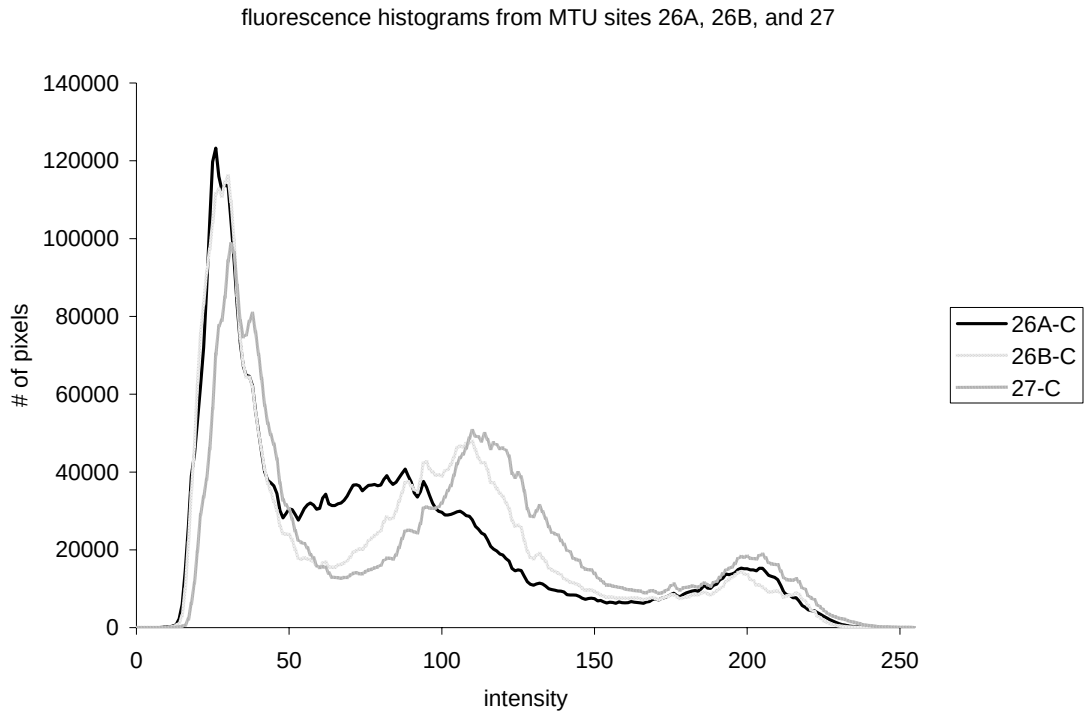

Figure D-35. Brightness histograms for epifluorescent mode images from Figures D-32 through D-34.

AIR VOID CHARACTERISTICS

Slabs from each pavement were polished and examined under a stereo OM in accordance with ASTM C457 Procedure B – Modified Point-Count Method. In addition to the standard procedure, the slabs were stained with a solution of potassium permanganate and barium chloride. The chemicals stain sulfate-bearing minerals, such as ettringite, pink. Over time, such minerals commonly occur as secondary growths in the entrained air voids. Often, entrained air voids in deteriorated concrete are completely filled with secondary ettringite. The stain assists in the identification of filled air voids that may otherwise be mistaken for hardened cement paste. In the equations used to determine the air-void system parameters, filled air voids that are identified as paste would be considered to offer no protection to freeze-thaw damage. It is controversial whether filled air voids can protect the paste against freeze-thaw damage, and thus, air-void system parameters are computed for both the concrete in its original state, and the concrete in its existing state. Table D-6 shows the results of the Modified Point-Count for the three sites. Figure D-36 plots the spacing factors for each site, along with dotted lines to represent the suggested range according to ASTM C457. Figure D-37 plots the void frequency for each site, along with dotted lines to represent the suggested range according to ASTM C457. Figure D-38 compares the aggregate, cement paste and air volume percentages as determined by point count to the volume percentages computed from the mix design.

Table D-6. Results of air void analyses for cores 26A-C, 26B-C, and 27-C.

MTU Core ID	26A-C	26B-D	27-C
Raw Data			
area analyzed (cm^2)	69.9	87.6	74.2
air stops	65	120	96
paste stops	368	389	336
aggregate stops	913	1202	1011
secondary ettringite stops	19	1	7
total stops	1365	1712	1450
traverse length (mm)	3565	4472	3787
# of air void intercepts	772	1496	1435
# of secondary ettringite filled intercepts	399	72	197
Results			
vol% aggregate	66.9	70.2	69.7
vol% air original	6.2	7.1	7.1
vol% air existing	4.8	7.0	6.6
vol% paste original	27.0	22.7	23.2
vol% paste existing	28.4	22.8	23.7
original void frequency (voids/m)	328	351	431
existing void frequency (voids/m)	217	335	379
original avg. chord length (mm)	0.187	0.202	0.165
existing avg. chord length (mm)	0.220	0.210	0.175
original specific surface (mm^{-1})	21.3	19.8	24.3
existing specific surface (mm^{-1})	18.2	19.1	22.9
original paste/air ratio	4.4	3.2	3.3
existing paste/air ratio	6.0	3.3	3.6
original spacing factor (mm)	0.204	0.162	0.134
existing spacing factor (mm)	0.276	0.170	0.156

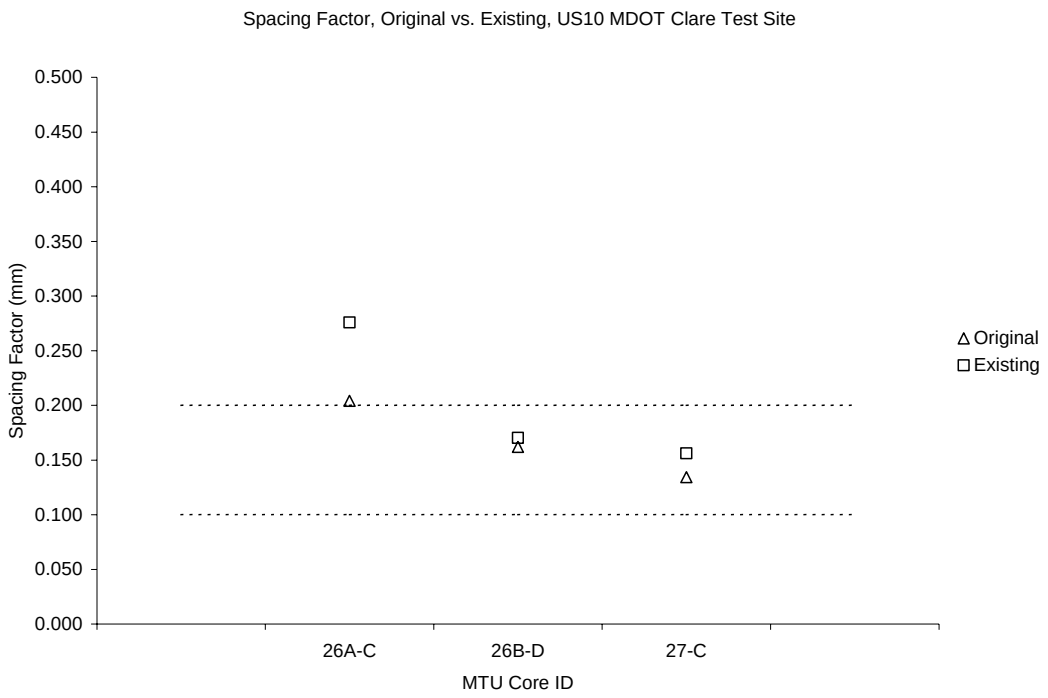

Figure D-36. Spacing factors plotted with dotted lines showing suggested values from ASTM C457.

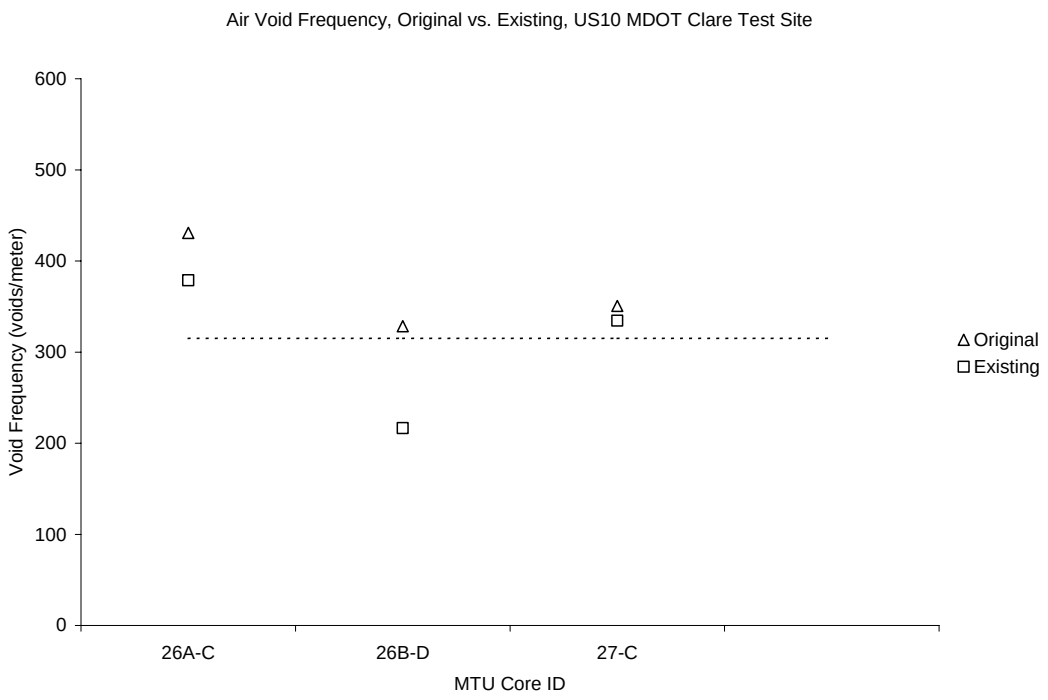

Figure D-37. Void frequencies plotted with dotted lines showing suggested values from ASTM C457.

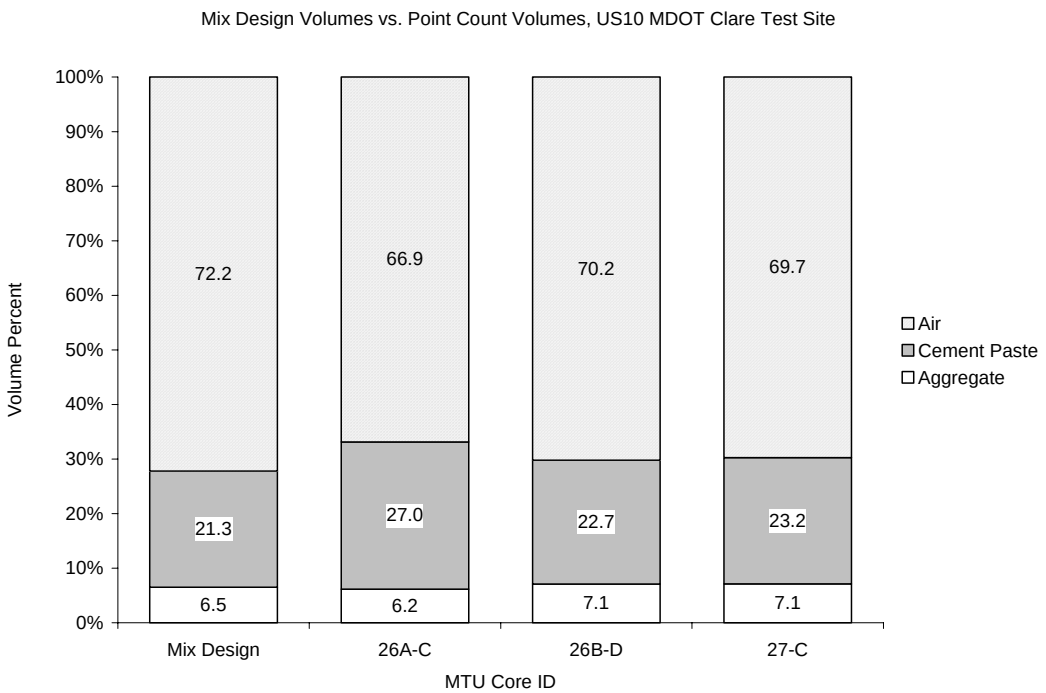

Figure D-38. Volume percentages from point counts compared to volume percentages computed from mix designs.

CONCLUSIONS

The MDOT US10 Clare Test Site was developed to evaluate various pavement design elements, and as such, the concrete used was designed to be the same throughout. Although the three sites all have the same mix design, the subbase materials used at the sites were not the same. Both Test Sites Nos. 26A and 26B utilized an asphalt treated permeable base, while Test Site No. 27 was supported on an aggregate base. The pavements are all currently in relatively poor condition, suffering joint deterioration that has been commonly been classified as "D-cracking." The following summarizes the microstructural observations made for these three test sites:

- Although the concrete was supposed to be the same, there are some noticeable differences between that in Test Site 26A and the other two test sites. The first observation is that the hydrated cement paste in Test Site 26A appears to be more dense, indicating that the *w/cm* for this site may have been less than for the other two sites. In addition, the overall original air content at Test Site 26A was also less than that at the other two sites.
- One primary distress mechanism appears to be ASR associated with the various cherts, impure cherty carbonates, and sandstones coarse aggregate particles. These aggregate particles have cracked, and copious quantities of alkali-silica reaction product are observed to be filling these cracks, which extend into the paste.

- A potentially contributing factor is aggregate freeze-thaw distress, since many of the cracked coarse aggregates are fine-grained and porous, sharing similar properties to aggregates known to be susceptible to freeze-thaw deterioration. Thus, it is possible that the cracking in the coarse aggregate is a result of freeze-thaw deterioration, and that the alkali-silica reaction occurred once the concrete fabric was compromised.
- Infilling of the air-void system with ettringnite is common, but more so in Test Site No. 26A. In this case, a marginal air-void system is becoming less capable of providing protection against freeze-thaw damage. Such infilling is a common feature in distress concrete, and it is unlikely that it is related to the initiation of the observed distress. Yet, it may contribute to the continuation of the distress once it has been initiated.

SITES 4, 19, AND 29: PAVEMENTS WITH BLAST FURNACE SLAG COARSE AGGREGATE

INTRODUCTION

The cores received from Test Site Nos. 4, 19, and 29 were from distressed pavements made with iron blast furnace slag coarse aggregate. Table D-7 summarizes the mix design information for the three sites. To investigate the sites, slabs were cut from the cores in a plane perpendicular to the pavement surface. Some of the slabs were polished and used for chemical staining and stereo OM, other slabs were cut into billets and prepared in thin section, and the rest of the slabs were crushed into powder to perform chemical extractions. Note that Test Site No. 4 is part of a special study, the report of which is presented in Appendix E.

CHEMICAL STAINS

A solution of sodium cobaltinitrite was applied to the polished slab surfaces to stain potassium-bearing alkali-silica gels yellow. The alkali-silica gel stain primarily affected the chert fine aggregate common to the three sites. Figure D-39 shows an example of a yellow-stained chert particle. A solution of barium chloride and potassium permanganate was used to stain sulfate-bearing minerals pink. The sulfate stain assisted with the identification of entrained air voids filled with secondary ettringite deposits observed during the ASTM C457 Modified Point Count. Figure D-40 depicts some pink-stained secondary ettringite filled air voids.

THIN SECTIONS

Two types of reactive fine aggregate particles were identified during the chemical staining procedures. Figures D-41a, D-41b, and D-41c show an example of a cracked reactive chert particle. The presence of a dense rim in contact with the cement paste, and cracks extending into the cement paste is typical of the chert particles in all three of the pavements. In addition to the chert particles, Test Site No. 29 had abundant siltstone fine aggregate particles similar to those of the fine aggregate from the US-23 MDOT Aggregate Test Site (Test Site Nos. 0 through 4A). Figures D-42a, D-42b, and D-42c show an example of a reactive siltstone particle between two chert particles. Siliceous fossils within the siltstone appear to be the reactive constituent. The siltstone particle shown is cracked, but the cracks do not extend into the surrounding cement paste.

Test Site No. 19 had the most severe cracking of the hydrated cement paste of the three sites. The cracks were often filled with alkali-silica reaction product. Figures D-43a, D-43b, and D-43c show some alkali-silica reaction product filled cracks with the gel apparently originating from a large chert particle. Figures D-44a, D-44b, and D-44c show a close-up of the crack filled with alkali-silica reaction product. Figure D-45 shows a back-scattered electron image of the same crack, and Figure D-46 is an x-ray energy spectrum collected from the alkali-silica reaction product shown in Figure D-45 with peaks for carbon, oxygen, aluminum, silicon, sulfur, chlorine, potassium, and calcium.

Table D-7. Volume percentage values computed from mix designs.

Test Site No.	4	19	29
Year Constructed	1992	1988/89	1976
kg/m^3 Cement	480	553	516
kg/m^3 Fly Ash	72	none	none
kg/m^3 Water	260	248	295
kg/m^3 Coarse	1399	2147	1427
kg/m^3 Fine	1551	1094	1679
w/cm	0.47	0.45	0.57
Vol% Cement Paste	25.6	24.4	26.1
Vol% Coarse Agg.	42.3	46.0	30.7
Vol% Fine Agg.	25.7	24.1	36.7
Vol% Air	6.5	5.5	6.5
Coarse Agg. No.	82-19	47-03	Trenton
Fine Agg. No.	63-54	63-04 63-47	81-57

Figure D-39. Yellow stained chert sand particle from Core 4-A.

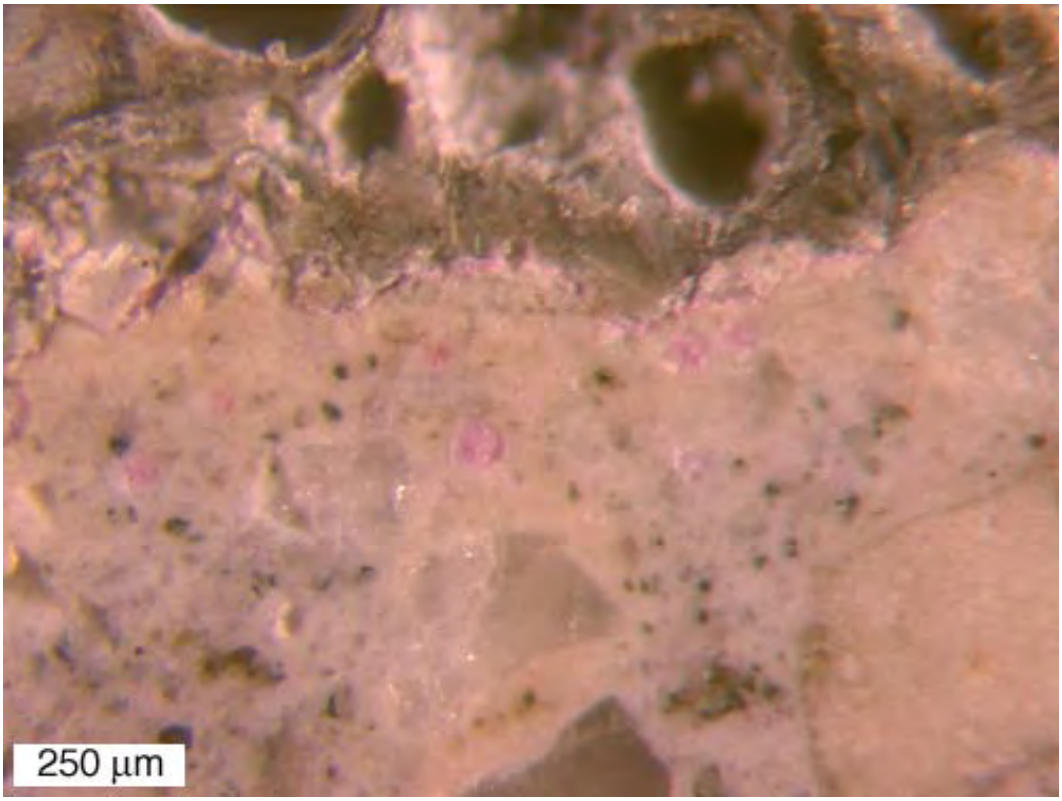

Figure D-40. A polished surface stained for sulfate minerals from Core 19-B.

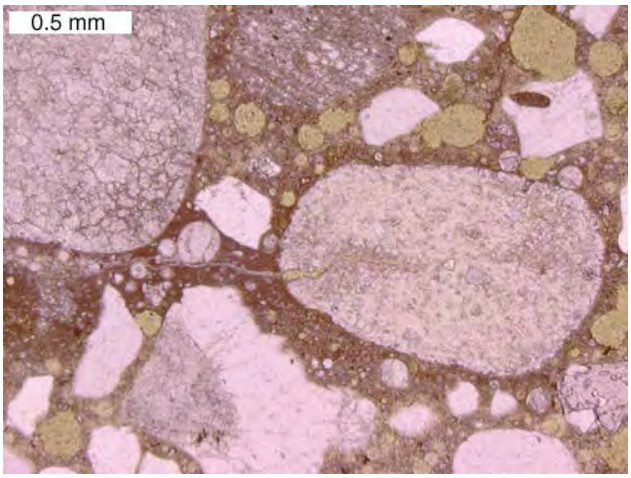

Figure D-41a. Thin-section view of a reactive chert sand particle from Core 4-A, plane-polarized light.

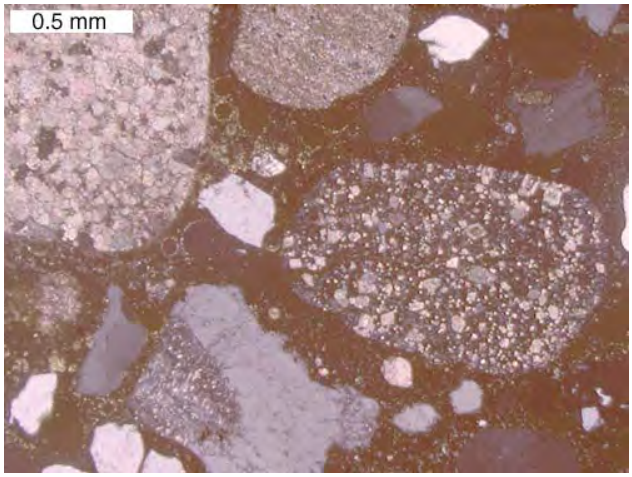

Figure D-41b. Thin-section view of a reactive chert sand particle from Core 4-A, cross-polarized light.

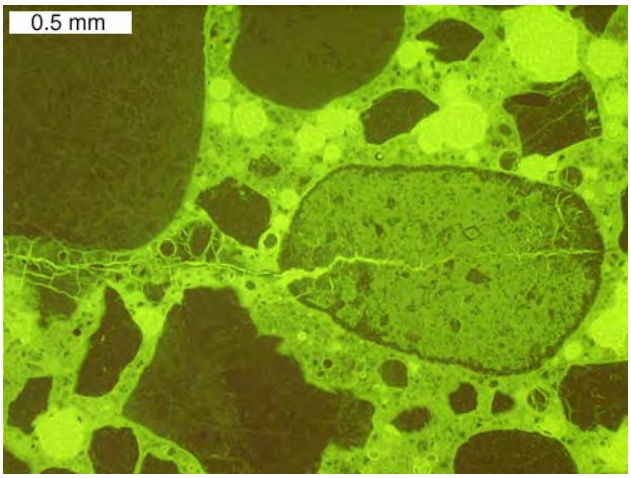

Figure D-41c. Thin-section view of a reactive chert sand particle from Core 4-A, epifluorescent mode.

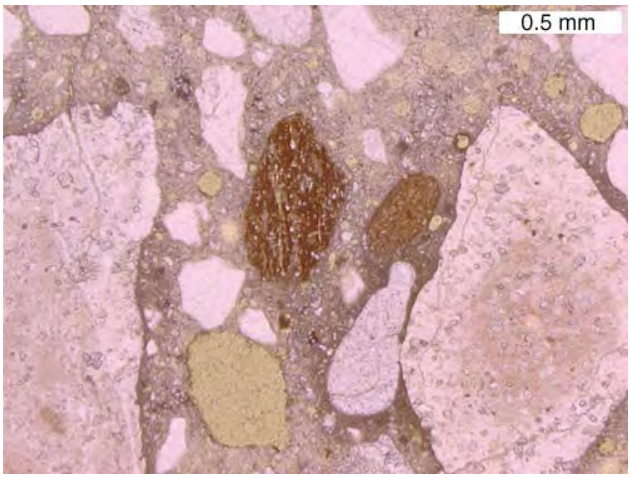

Figure D-42a. Thin-section view of a reactive siltstone sand particle, (center) with reactive chert particles on either side, Core 4-A, plane-polarized light.

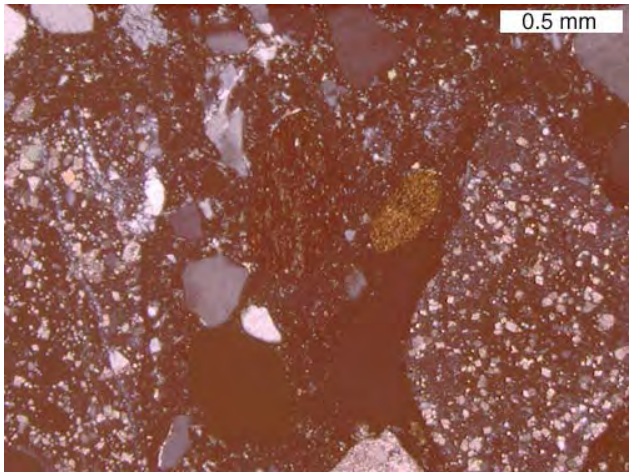

Figure D-42b. Thin-section view of a reactive siltstone sand particle, (center) with reactive chert particles on either side, Core 4-A, cross-polarized light.

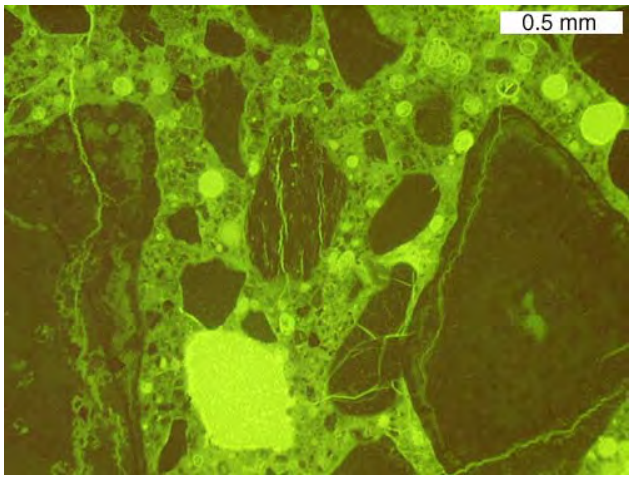

Figure D-42c. Thin-section view of a reactive siltstone sand particle, (center) with reactive chaert particles on either side, Core 4-A, epifluorescent mode.

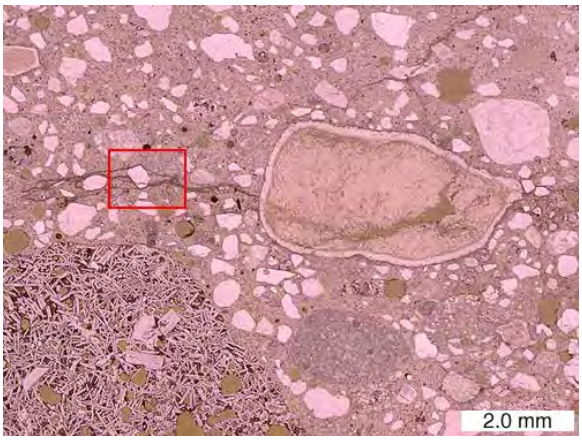

Figure D-43a. Thin-section view of a reactive chert sand particle with cracks extending into surrounding cement paste, Core 19-B, red box shows area of close-up in Figure D-44a, plane-polarized light.

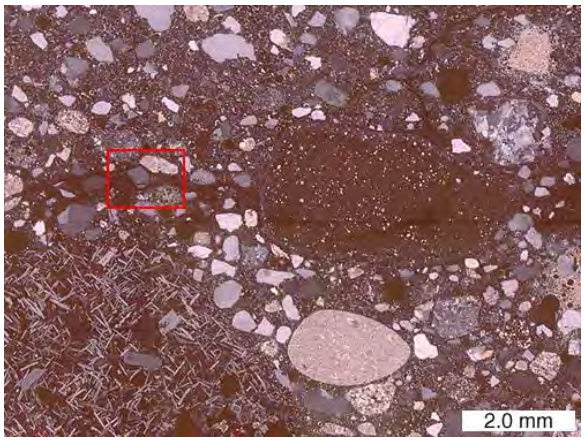

Figure D-43b. Thin-section view of a reactive chert sand particle with cracks extending into surrounding cement paste, Core 19-B, red box shows area of close-up in Figure D-44b, cross-polarized light.

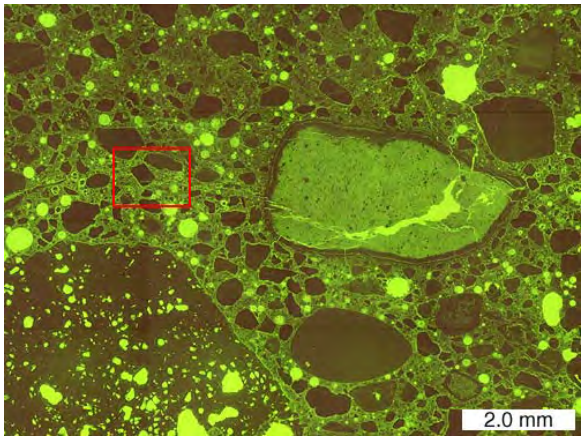

Figure D-43c. Thin-section view of a reactive chert sand particle with cracks extending far into the surrounding cement paste, Core 19-B, red box shows area of close-up in Figure D-44c, epifluorescent mode.

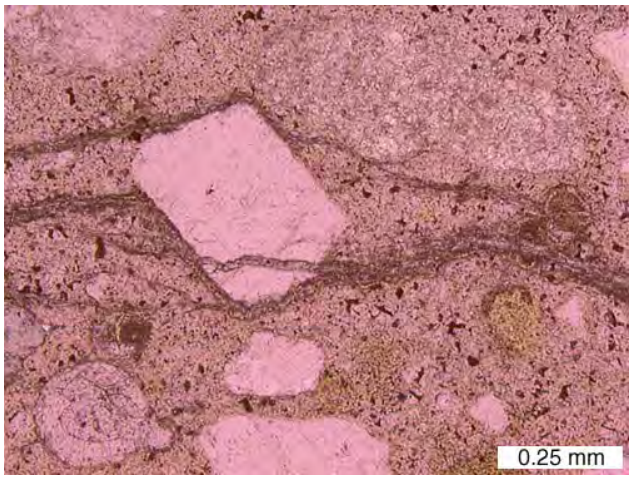

Figure D-44a. Close-up of area shown in Figure D-43a showing alkali-silica reaction product filled cracks and voids, Core 19-B, plane-polarized light.

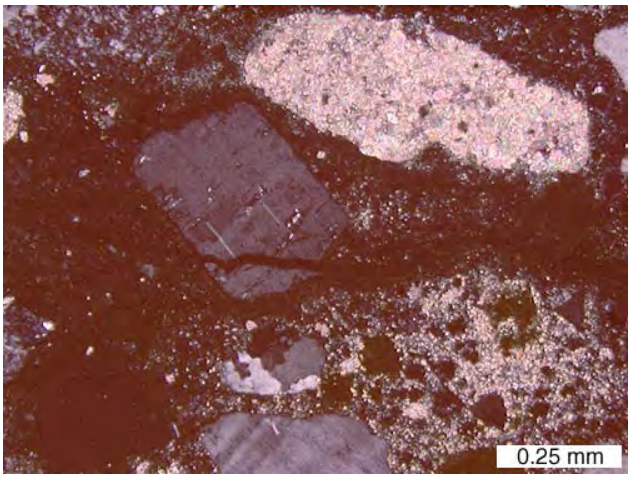

Figure D-44b. Close-up of area shown in Figure D-44b showing alkali-silica reaction product filled cracks and voids, Core 19-B, cross-polarized light.

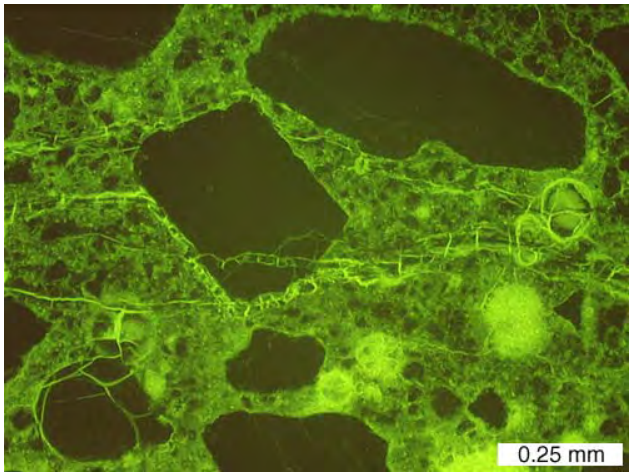

Figure D-44c. Close-up of area shown in Figure D-44c showing alkali-silica reaction product filled cracks and voids, Core 19-B, epifluorescent mode.

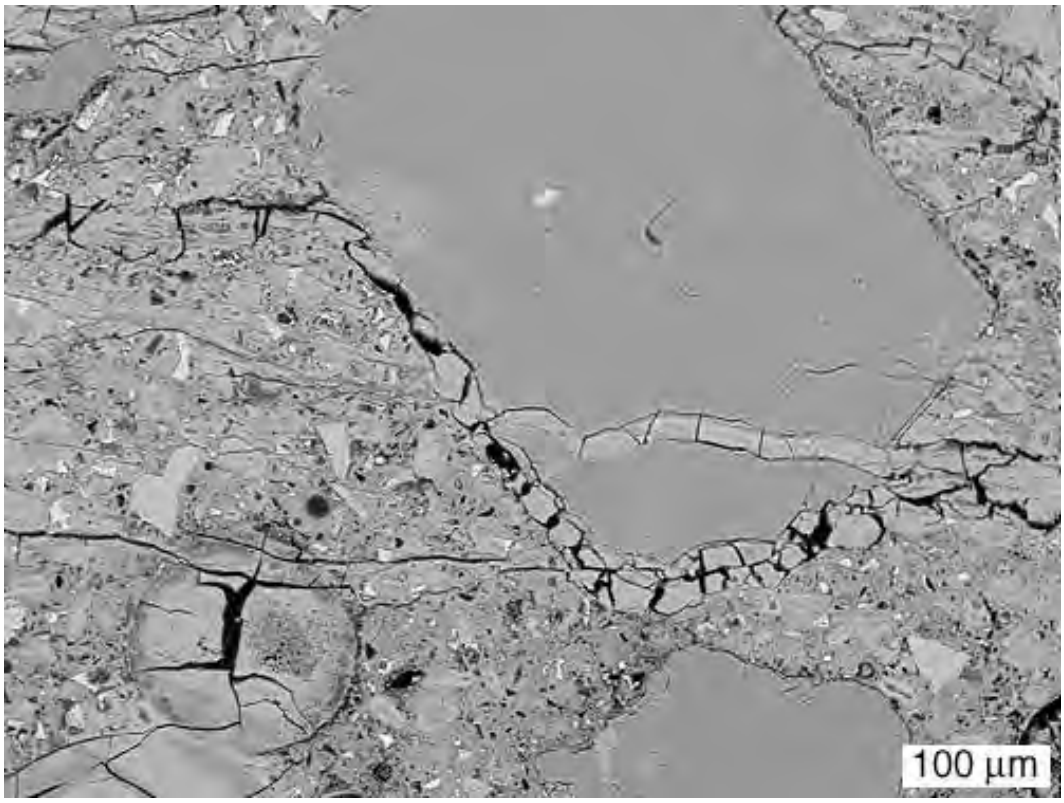

Figure D-45. Back-scattered electron image of cracks and void filled with alkali-silica reaction product, Core 19-B.

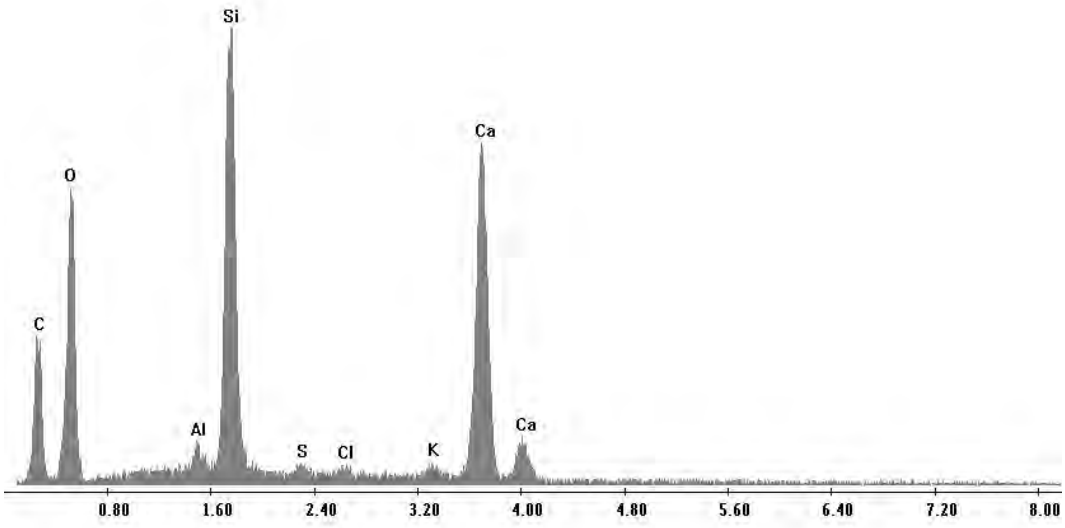

Figure D-46. X-ray energy spectrum collected from alkali-silica reaction product shown in Figure D-45.

It is noted that a peak for carbon is always present regardless of the concentration of carbon in the sample due to the thin layer of carbon that was evaporated on to the sample surface to prevent charge build-up during the electron microscope investigation.

In addition to the abundant alkali-silica reaction product filled cracks at Test Site No. 19, there were also many cracks filled with ettringite. Figures D-47a, D-47b, and D-47c show some ettringite filled cracks. Figures D-48 and D-49 are back-scattered electron images of large cracks running along the contact between slag coarse aggregate and the cement paste. Figure D-50 is an x-ray energy spectrum collected from the ettringite. Figure D-51 is a close-up of a region in Figure D-49 showing calcium sulfide dendrites in the slag aggregate.

Often, in all three pavements, the cement paste in the immediate vicinity of slag coarse aggregate particles appears darker than the rest of the cement paste. At the cement paste/slag aggregate interface the cement paste is denser and partially hydrated cement grains are very abundant. Calcium hydroxide crystals are also often found in the air voids near slag aggregate particles. Figures D-52a, D-52b, and D-52c show a cement paste/slag aggregate interface. The calcium hydroxide filled air voids appear bright yellow in Figure D-52b. Figures D-53a, D-53b, and D-53c are close-ups of a calcium hydroxide filled void and many partially hydrated cement grains. In Figure D-53a, a green coloration is associated with the ferrite and aluminate phases of the cement grains.

CHEMICAL EXTRACTIONS

A gravimetric procedure of sulfate determination was used according to British Standard 1881:Part 124. Methods for Analysis of Hardened Concrete: 1988. The weight percent SO_3 computed from the mix design assumes 3.5% by weight SO_3 for the cement and 4.5% by weight of the fly ash. The results of the sulfate determinations, expressed in terms of SO_3, are presented in Table D-8. Figure D-54 plots the computed SO_3 wt% next to the extracted SO_3 wt% for each of the sites. In all three of the sites, the extraction values exceeded the computed values.

A standard technique for alkali extraction from hardened concrete was not available, so an ammonium acetate extraction technique developed for the determination of exchangeable and soluble sodium and potassium in soils was adopted. The concentrations of potassium and sodium were determined by an inductively coupled plasma emission spectrophotometer. The results from the test are expressed in weight percent elemental sodium and weight percent elemental potassium. In Table D-9, the results were converted to the industry convention of kilograms of "Na_2O equivalent" per cubic meter of concrete, based on the total mass from the mix designs. The recalculation to kilograms of "Na_2O equivalent" per cubic meter of concrete allows comparisons to be made with industry standards for limiting total alkalis in the mixture. The Canadian standards specifying a maximum of 3.0 kg/m^3 Na_2O equivalent for mild protection, 2.2 kg/m^3 Na_2O equivalent for moderate protection, and 1.7 kg/m^3 Na_2O equivalent for strong protection. Figure D-55 plots the Na_2O equivalent values from extraction for all of the sites, along with dotted lines showing the Canadian protection levels.

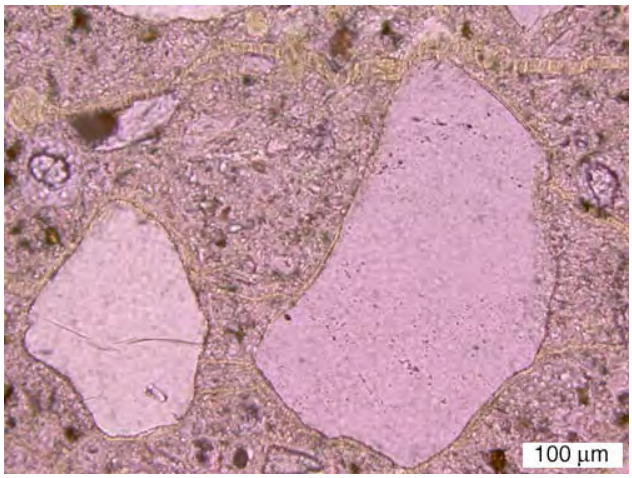

Figure D-47a. Thin-section view of ettringite filled crack along slag aggregate/cement paste interface, Core19-B, plane-polarized light.

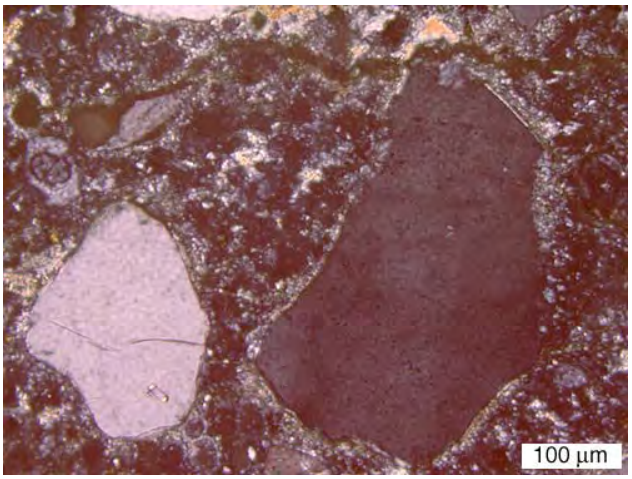

Figure D-47b. Thin-section view of ettringite filled crack along slag aggregate/cement paste interface, Core19-B, cross-polarized light.

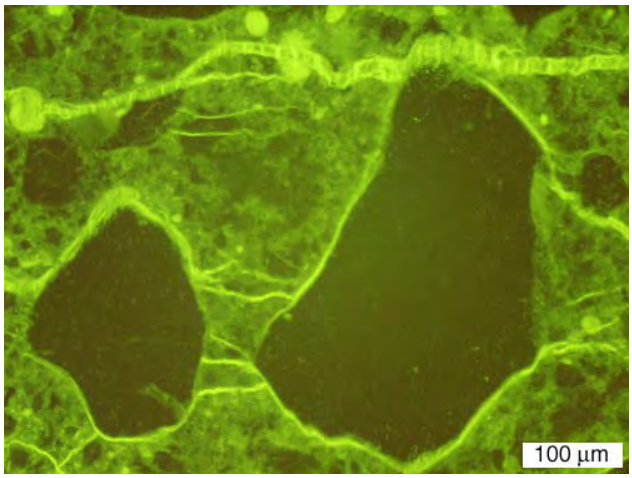

Figure D-47c. Thin-section view of ettringite filled crack along slag aggregate/cement paste interface, Core19-B, epifluorescent mode.

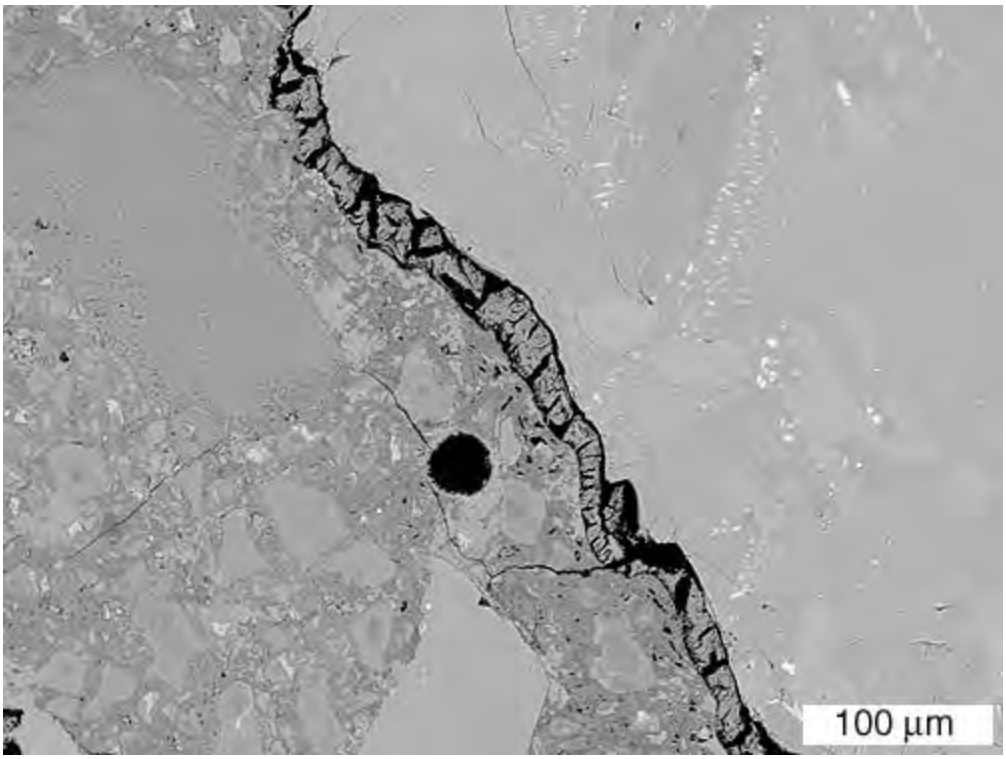

Figure D-48. Back-scattered electron image of ettringite filled crack along slag aggregate/cement paste interface, Core 19-B.

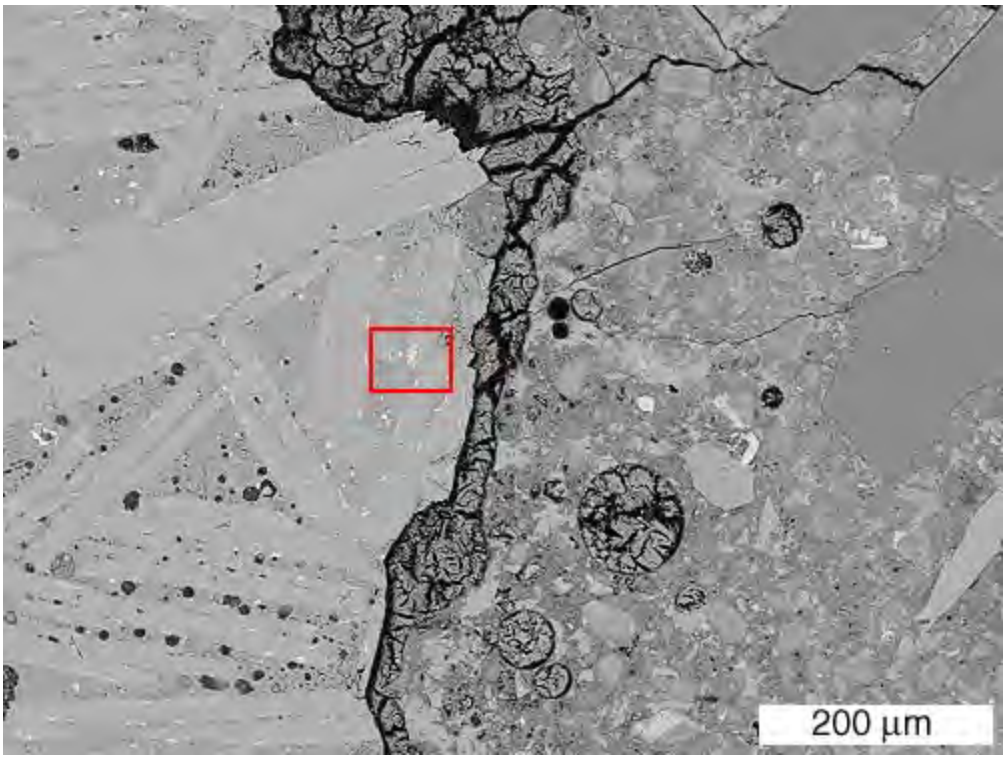

Figure D-49. Back-scattered electron image of ettringite filled crack along slag aggregate/cement paste interface in Core 19-B, red box shows area of close-up in Figure D-51.

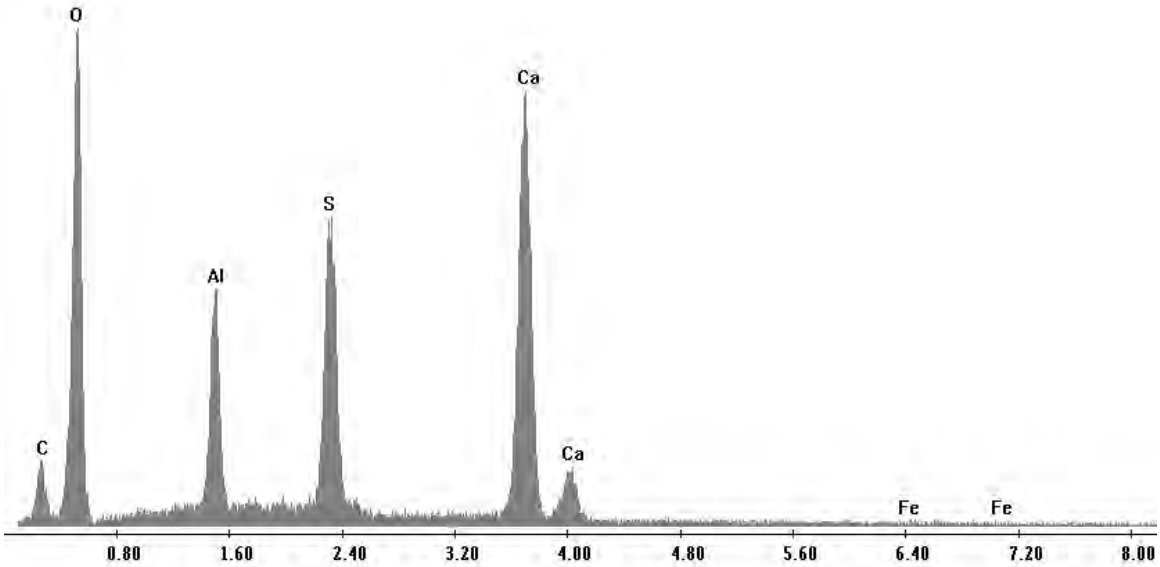

Figure D-50. X-ray energy spectrum collected from ettringite filled crack shown in Figure D-49.

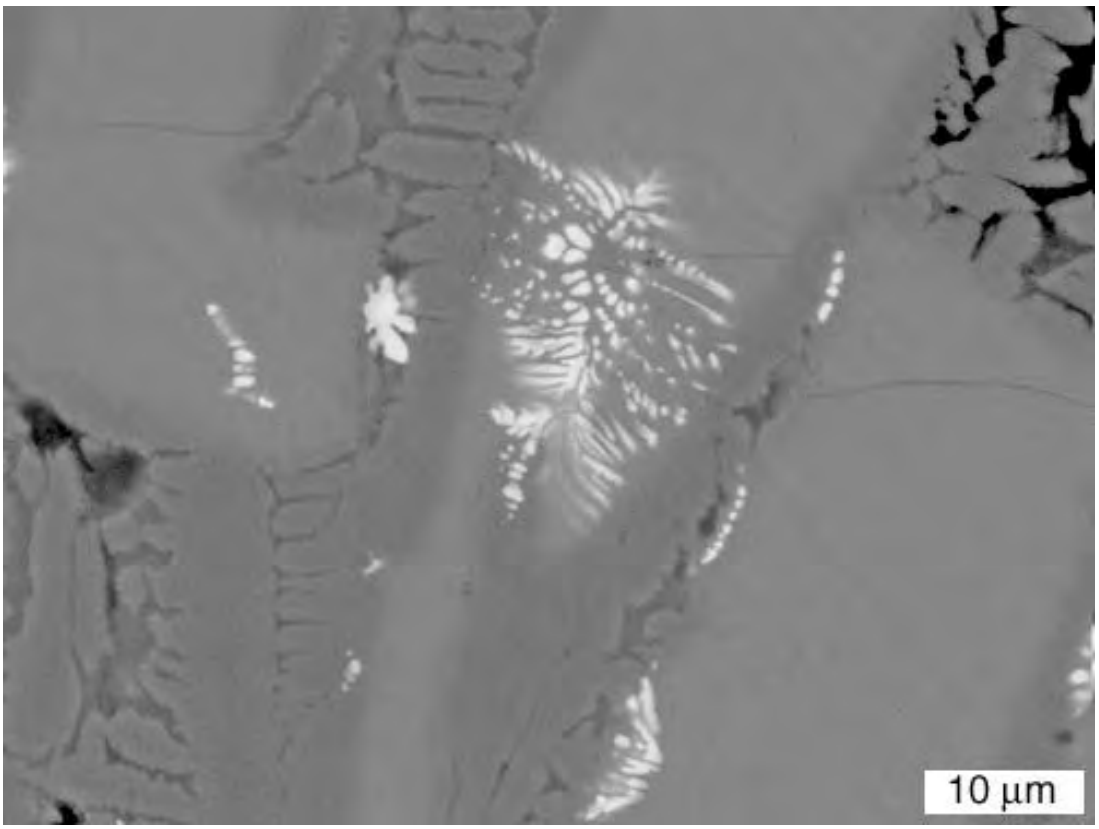

Figure D-51. Close-up of area outlined in red in Figure D-49 with calcium sulfide dendrites in slag aggregate, Core 19-B.

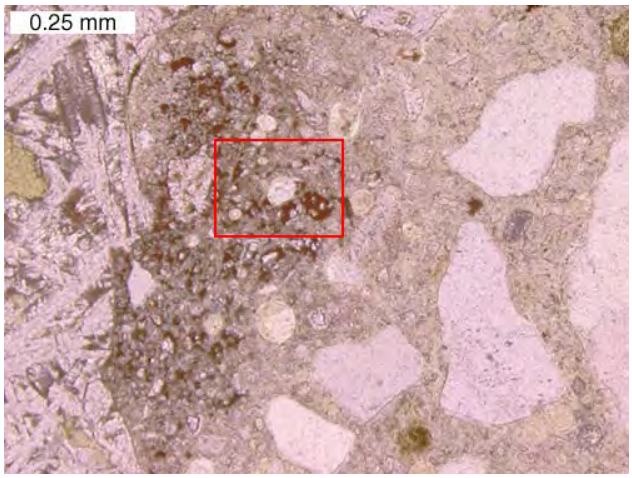

Figure D-52a. Thin-section view of cement paste near contact with slag aggregate, red box shows area of close-up in Figure D-53a, Core 29-A, plane-polarized light.

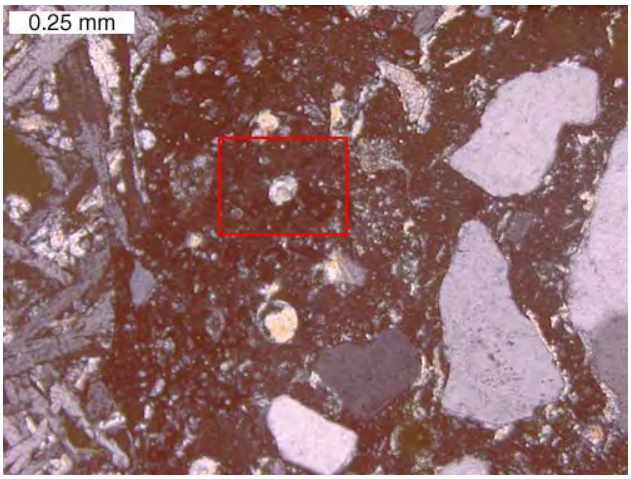

Figure D-52b. Thin-section view of cement paste near contact with slag aggregate, red box shows area of close-up in Figure D-53b, Core 29-A, cross-polarized light.

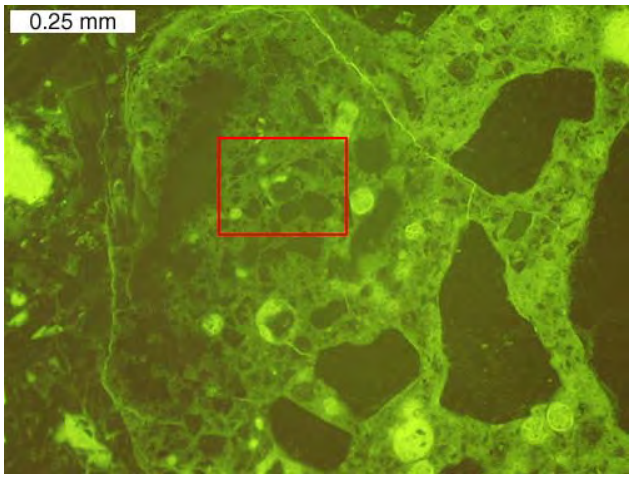

Figure D-52c. Thin-section view of cement paste near contact with slag aggregate, red box shows area of close-up in Figure D-53c, Core 29-A, epifluorescent mode.

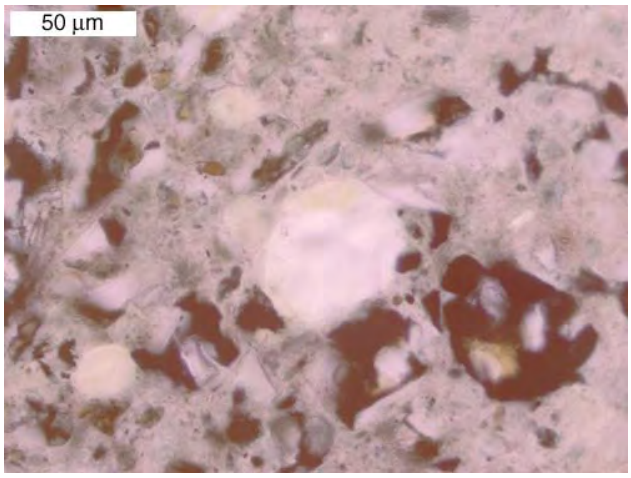

Figure D-53a. Close-up of area outlined in red in Figure D-52a, Core 29-A, plane-polarized light.

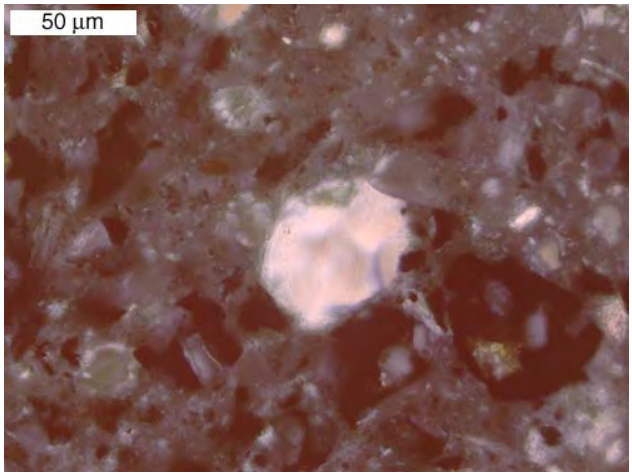

Figure D-53b. Close-up of area outlined in red in Figure D-52b, Core 29-A, cross-polarized light.

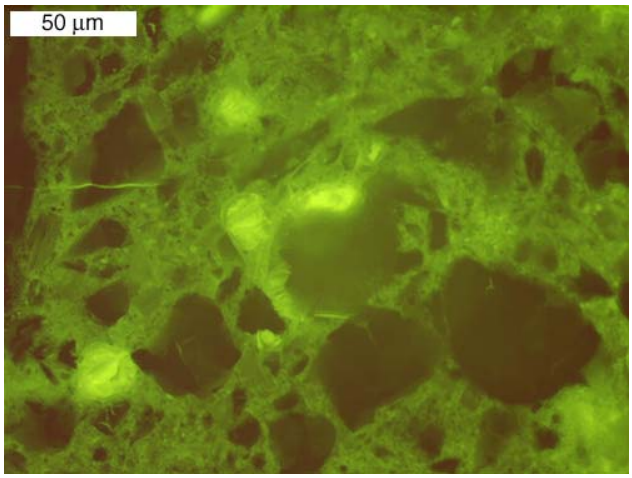

Figure D-53c. Close-up of area outlined in red in Figure D-52c, Core 29-A, epifluorescent mode.

Table D-8. Results of sulfate extractions.

MTU Core ID	Computed Wt% SO_3	Extracted Wt% SO_3
4-A	0.53	0.67
19-B	0.48	0.68
29-A	0.46	0.57

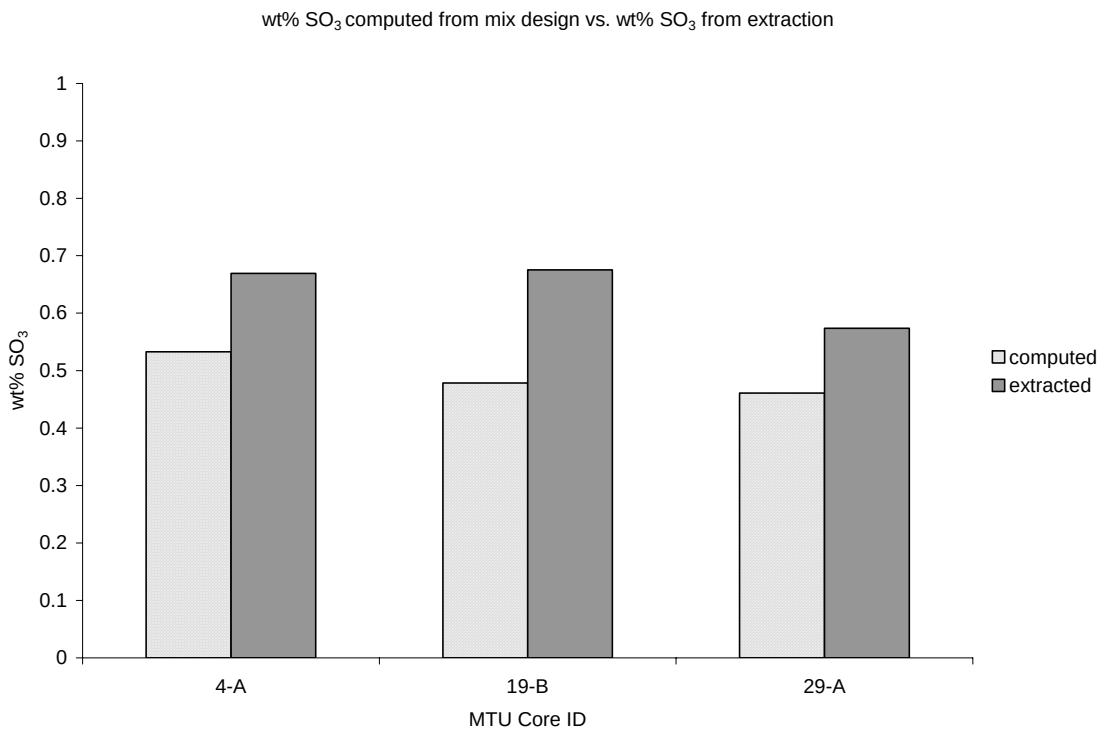

Figure D-54. Wt% SO_3 values from extraction compared to wt% SO_3 values computed from the mix design.

Table D-9. Results of alkali extractions.

MTU Core ID	Wt% Na	Wt% K	Na_2O Equivalent kg/m^3
4-A	0.054	0.025	2.05
19-B	0.032	0.044	1.87
29-A	0.030	0.038	1.62

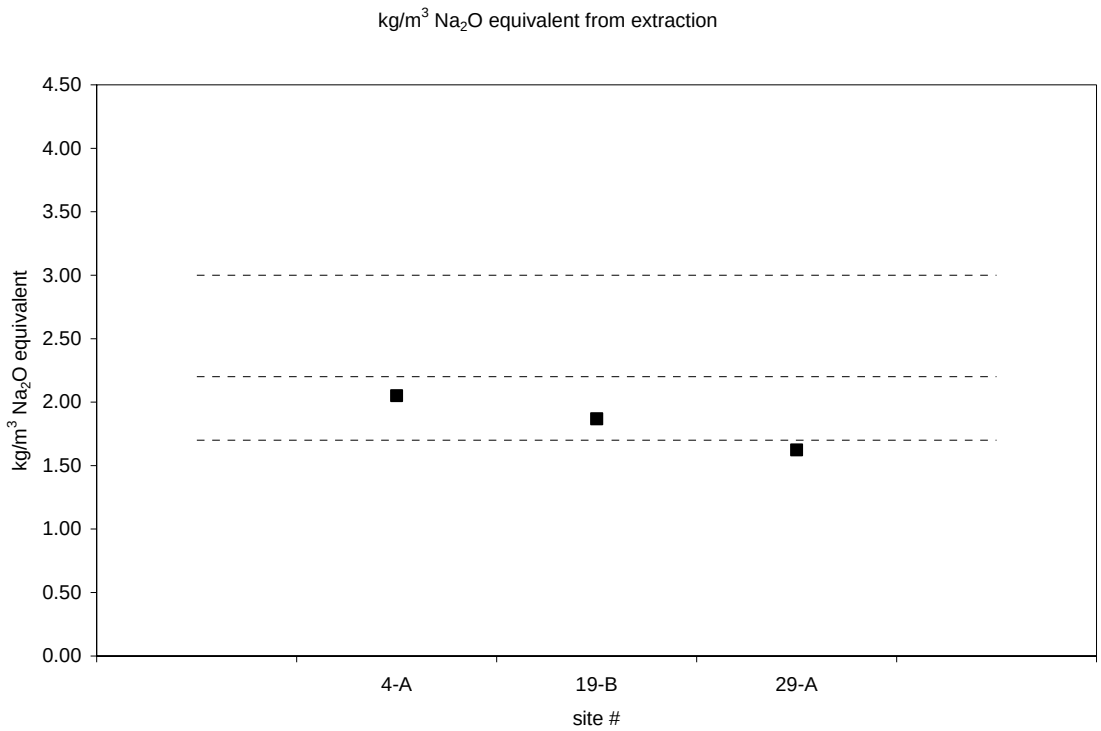

Figure D-55. Na_2O equivalent kg/m^3 values from extraction compared to Na_2O equivalent kg/m_3 values computed from the mix design.

AIR VOID CHARACTERISTICS

Slabs from each pavement were polished and examined under a stereo OM in accordance with ASTM C457 Procedure B – Modified Point-Count Method. In addition to the standard procedure, the slabs were stained with a solution of potassium permanganate and barium chloride. The chemicals stain sulfate-bearing minerals, such as ettringite, pink. Over time, such minerals commonly occur as secondary growths in the entrained air voids. Often, entrained air voids in deteriorated concrete are completely filled with secondary ettringite. The stain assists in the identification of filled air voids that may otherwise be mistaken for hardened cement paste. In the equations used to determine the air-void system parameters, filled air voids that are identified as paste would be considered to offer no protection to freeze-thaw damage. It is controversial whether filled air voids can protect the paste against freeze-thaw damage, and thus, air-void system parameters are computed for both the concrete in its original state, and the concrete in its existing state.

Table D-10 shows the results of the Modified Point-Count for the three sites. Figure D-56 plots the spacing factors for each site, along with dotted lines to represent the suggested range according to ASTM C457. Figure D-57 plots the void frequency for each site, along with dotted lines to represent the suggested range according to ASTM C457. Figure D-58 compares the aggregate, cement paste and air volume percentages as determined by point count to the volume percentages computed from the mix design.

CONCLUSIONS

The cores received from Test Site Nos. 4, 19, and 29 were from distressed pavements made with iron blast furnace slag coarse aggregate. They were constructed between 1976 and 1992, and are located in the Southeastern part of the Lower Peninsula. One of the test sites (Test Site No. 4) was ultimately included in a special study, the report of which is presented in Appendix E. The results of the microstructural evaluation can be summarized as follows:

- In all three pavement sections, reactive chert particles that are a constituent in the fine aggregate were aggressively and deleteriously alkali-silica reactive, leading to the formation of significant reaction product and associated cracking in the hydrated cement paste. This was true even though the extracted alkali contents of the two of the three sections would indicate “moderate” protection against ASR. The third section (Test Site No. 29) had an even lower extracted alkali content that would offer “strong” protection against ASR, but it was built in 1976 which may indicate that ultimately the deleterious reaction with the chert will occur given enough time. Only one section had fly ash (Test Site No. 4) and this was a Class C fly ash.
- In all cases, the extracted sulfate contents were in excess of that predicted from the mixture design. In addition, the degree of crack and air void infilling with ettringite was high. It was also observed that in many cases the calcium sulfide dendrites located near the aggregate-hydrated cement paste interface were “empty”, indicating that potential dissolution of the calcium sulfide had occurred. This is one explanation

Table D-10. Results of ASTM C457 Modified Point Counts.

MTU Core ID	4-A	19-B	29-A
Raw Data			
area analyzed (cm^2)	94.9	69.4	100.2
air stops	117	133	150
paste stops	294	466	429
aggregate stops	921	747	841
secondary ettringite stops	18	10	5
total stops	1350	1356	1425
traverse length (mm)	4134	3542	4363
# of air void intercepts	1318	1066	1878
# of secondary ettringite filled intercepts	448	77	404
Results			
vol% aggregate	68.2	55.1	59.0
vol% air original	10.0	10.5	10.9
vol% air existing	8.7	9.8	10.5
vol% paste original	21.8	34.4	30.1
vol% paste existing	23.1	35.1	30.5
original void frequency (voids/m)	427	323	523
existing void frequency (voids/m)	319	301	430
original avg. chord length (mm)	0.234	0.327	0.208
existing avg. chord length (mm)	0.272	0.326	0.245
original specific surface (mm^{-1})	17.1	12.2	19.2
existing specific surface (mm^{-1})	14.7	12.3	16.4
original paste/air ratio	2.2	3.3	2.8
existing paste/air ratio	2.7	3.6	2.9
original spacing factor (mm)	0.127	0.266	0.144
existing spacing factor (mm)	0.181	0.292	0.177

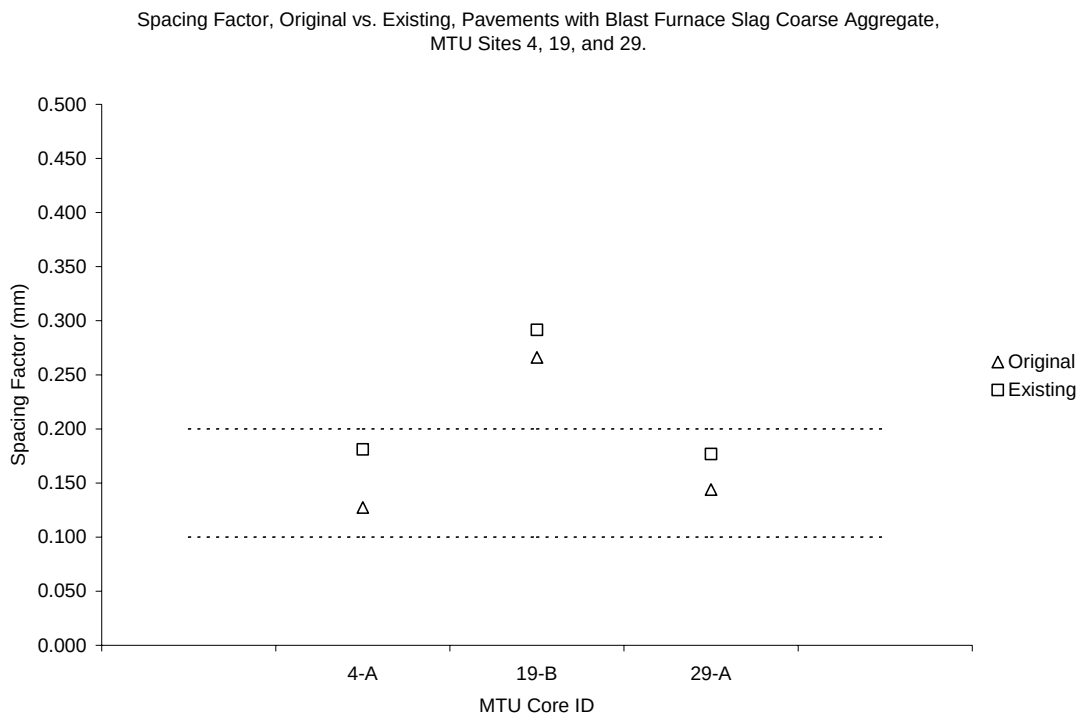

Figure D-56. Spacing factors plotted with dotted lines showing suggested values from ASTM C457.

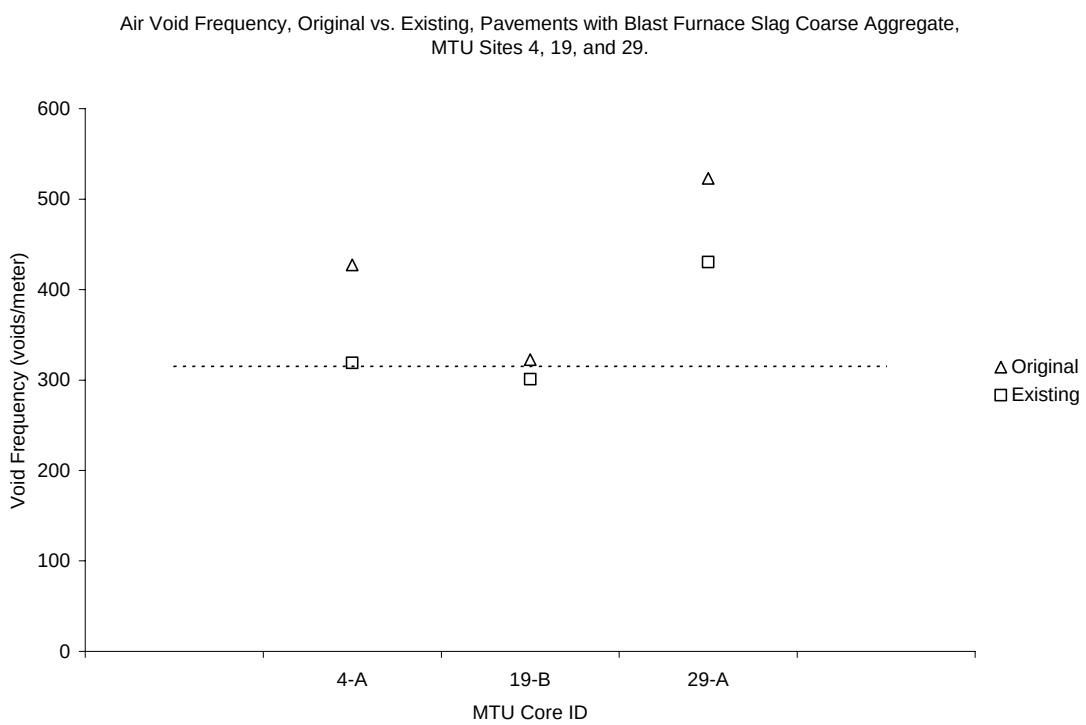

Figure D-57. Void frequencies plotted with dotted lines showing suggested values from ASTM C457.

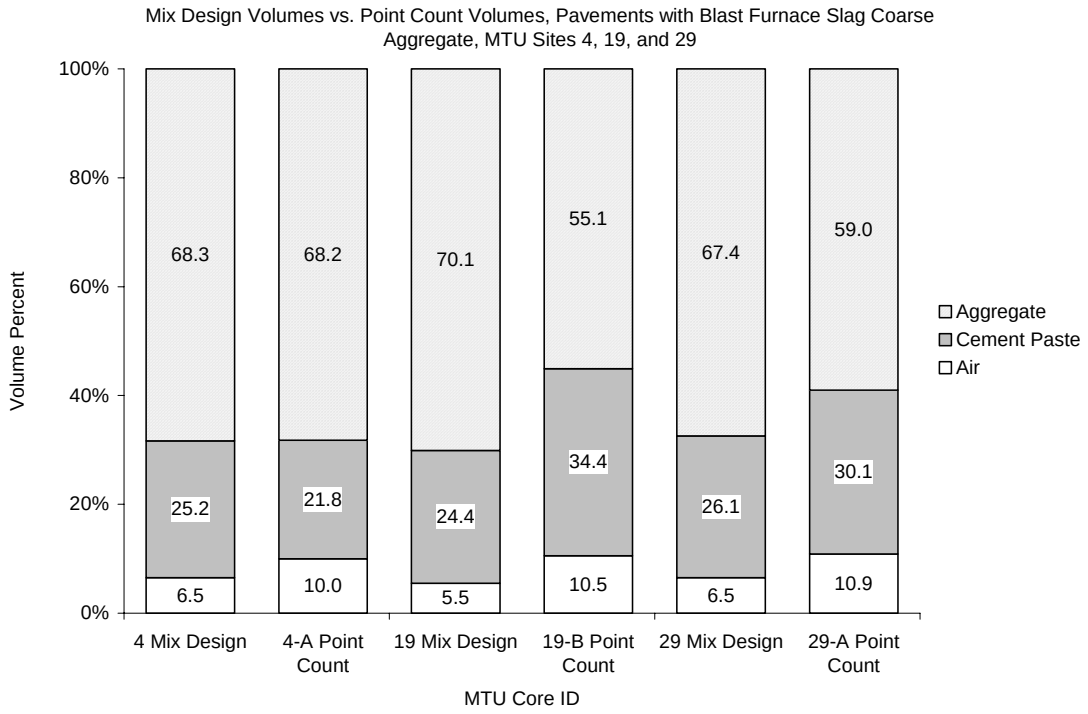

Figure D-58. Volume percentages from point counts compared to volume percentages computed from mix designs.

for the origination of the excess sulfates measured through extractions, although further work needs to be conducted to investigate this further.

- Often, in all three pavements, the cement paste in the immediate vicinity of slag coarse aggregate particles appears darker than the rest of the cement paste, primarily due to the presence of partially hydrated cement grains that are very abundant. In addition, calcium hydroxide crystals are also often found in the air voids near slag aggregate particles. Further, a green coloration is associated with the ferrite and aluminate phases of the cement grains near the interface. The implication of these findings is currently unknown, but without question some chemical interactions are occurring between the slag coarse aggregate and the hydrated cement paste/pore solution in the vicinity of the paste-aggregate interface.
- At all three test sites, the measured original air content was significantly higher than that specified (10 percent or greater). Even though, one test site (Test Site No. 19) had an original spacing factor that would provide only marginal protection against paste freeze-thaw damage. Further, the infilling with ettringite has significantly altered the measured air-void system parameters, potentially reducing paste freeze-thaw durability.

SITES 12, 22, AND 28, PAVEMENTS WITH NATURAL GRAVEL COARSE AGGREGATE

INTRODUCTION

The cores received from Test Site Nos. 12, 22, and 28 were from distressed pavements. Table D-11 summarizes the mix design information for the three sites. Figures D-59, D-60 , and D-61 are provided to give a general overview of the different pavements. To investigate the sites, slabs were cut from the cores in a plane perpendicular to the pavement surface. The slabs were polished and used for chemical staining and stereo OM.

CHEMICAL STAINS

A solution of sodium cobaltinitrite was applied to the polished slab surfaces to stain potassium-bearing alkali-silica gels yellow. The slabs prepared from Test Site No. 22 were not significantly affected by the sodium cobaltinitrite stain. Chert particles, both in the fine and coarse aggregate fractions were stained yellow in slabs prepared from Test Site Nos. 12 and 28. Figure D-62 is an example of a yellow-stained chert particle. In general, cracking was not associated with the fine chert particles. However, cracking was sometimes associated with coarse chert particles. Figure D-63 shows an example of a yellow-stained chert coarse aggregate particle and related cracking. A solution of barium chloride and potassium permanganate was used to stain sulfate-bearing minerals pink. The sulfate stain assisted with the identification of entrained air voids filled with secondary ettringite deposits observed during the ASTM C457 Modified Point Count. Figure D-64 depicts some pink-stained secondary ettringite filled air voids.

MACRO-CRACKING

All of the sites contained large coarse aggregate particles (by today's standards) with an estimated top size estimated of least 38 mm (1.5 inches). Relatively porous carbonate aggregates of this size were frequently cracked. Figures D-65a and D-65b show cracking typical of the carbonate aggregates from Test Site No. 22. Figures D-66a and D-66b show an entire polished slab taken from the joint at Test Site No. 12. The core that provided the slab shown in Figures D-66a and D-66b was received in several pieces, and was epoxied together prior to slabbing. The length of the core shown in Figures D-66a and D-66b is not representative of the true pavement depth because the base of the pavement was so deteriorated that a complete intact core could not be retrieved. A large carbonate aggregate near the base of the slab is severely cracked.

AIR VOID CHARACTERISTICS

Slabs from each pavement were polished and examined under a stereo OM in accordance with ASTM C457 Procedure B – Modified Point-Count Method. In addition to the standard procedure, the slabs were stained with a solution of potassium permanganate and barium chloride. The chemicals stain sulfate-bearing minerals, such as ettringite,

Table D-11. Volume percentage values computed from mix designs.

Test Site No.	**12**	**22**	**28**
Year Constructed	1957	1957	1960
kg/m^3 Cement	300	301	231
kg/m^3 Fly Ash	0	0	0
kg/m^3 Water	155	162	108
kg/m^3 Coarse	1437	1260	998
kg/m^3 Fine	718	644	478
w/cm	0.52	0.54	0.47
Vol% cement paste	22.4	25.1	23.4
Vol% Coarse Agg.	47.4	45.5	47.7
Vol% Fine Agg.	24.7	23.4	23.0
Vol% Air	5.5	6.0	6.0
Coarse Agg. No.	34-36	49-44	67-02
Fine Agg. No.	34-36	49-44	67-02

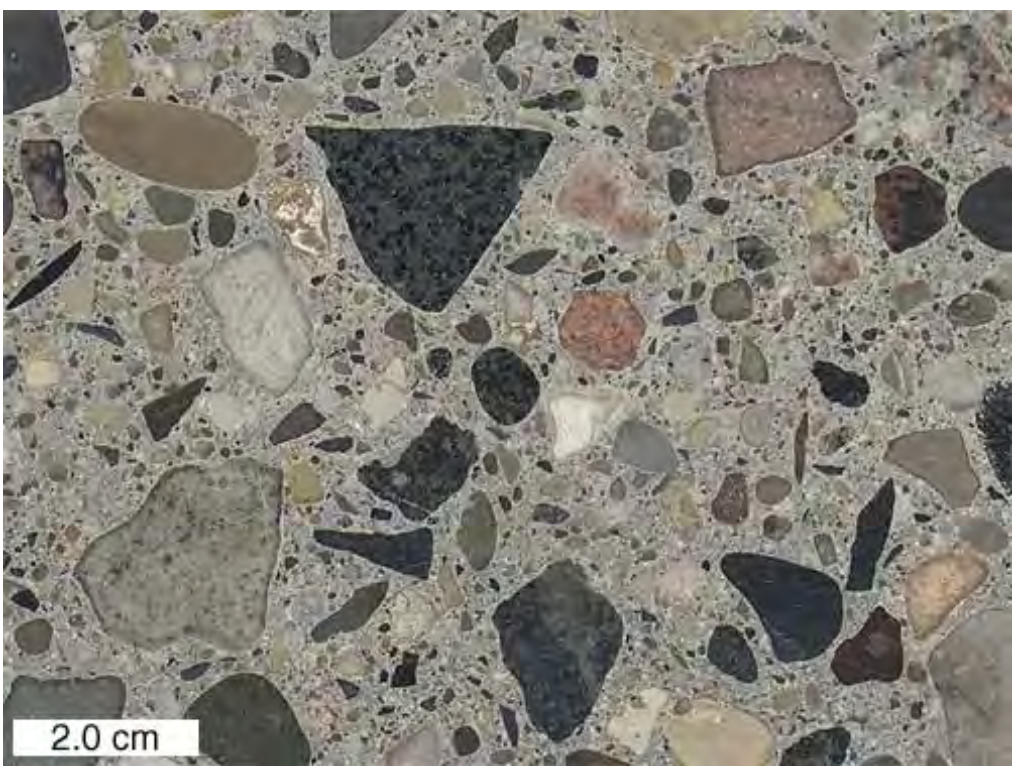

Figure D-59. View of polished slab from Core 12-C.

Figure D-60. View of polished slab from Core 22-C.

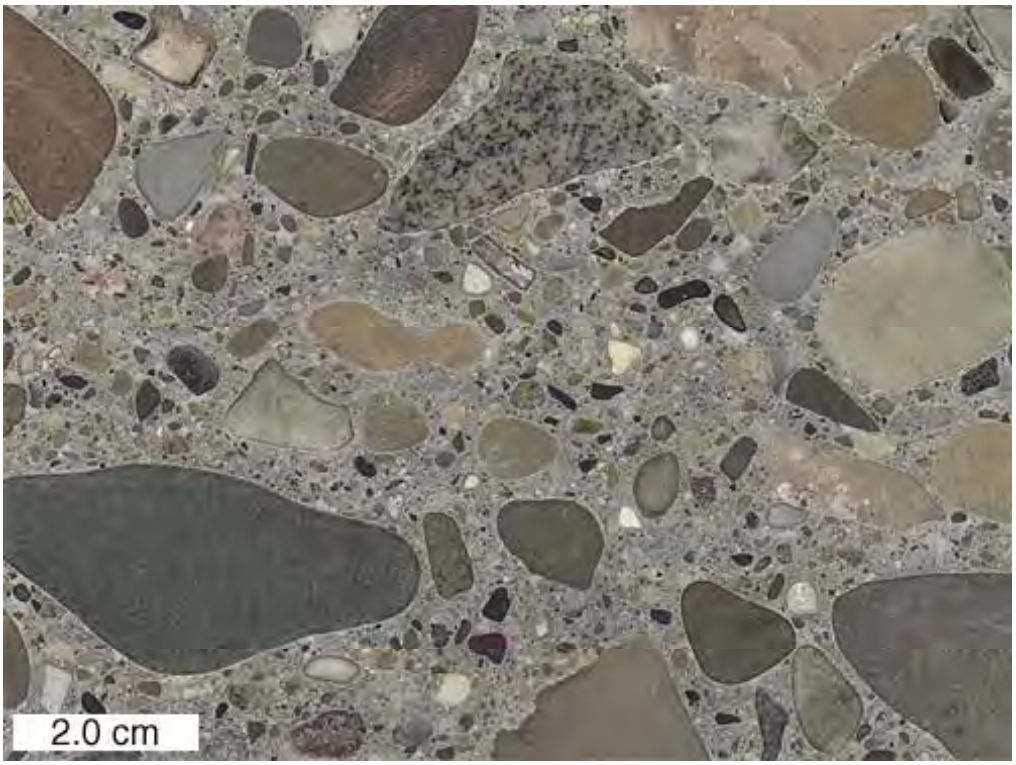

Figure D-61. View of polished slab from Core 28-B.

Figure D-62. Yellow stained chert fine aggregate particle, Core 28-B.

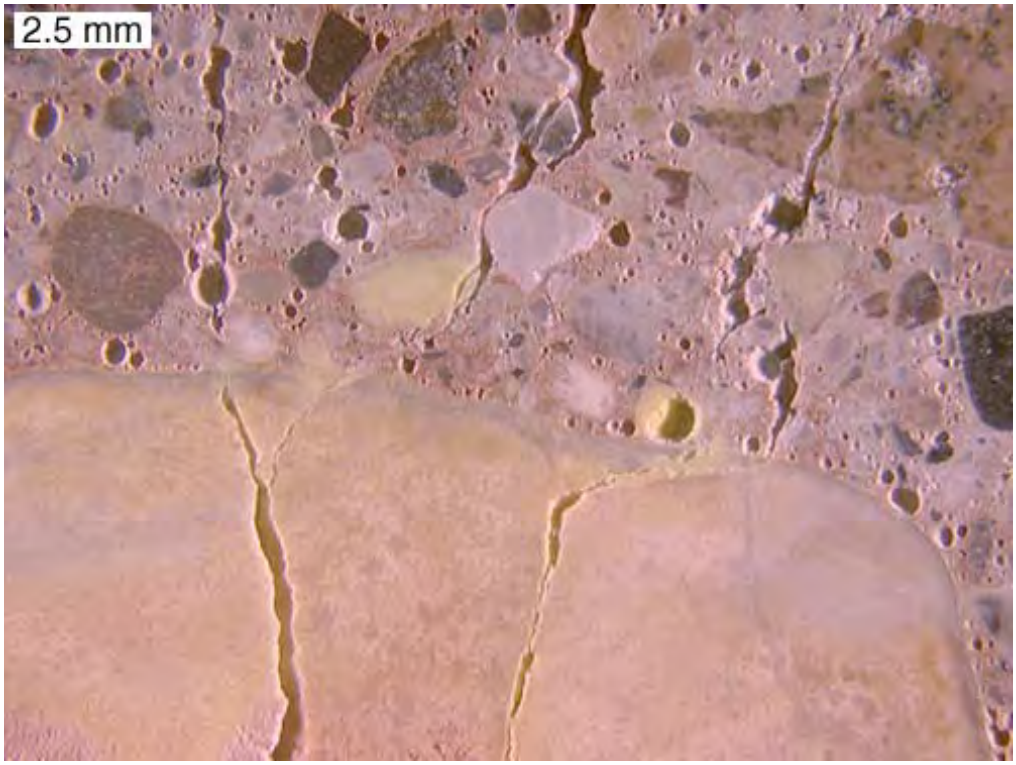

Figure D-63. Yellow stained chert coarse aggregate with cracks, core 12-C.

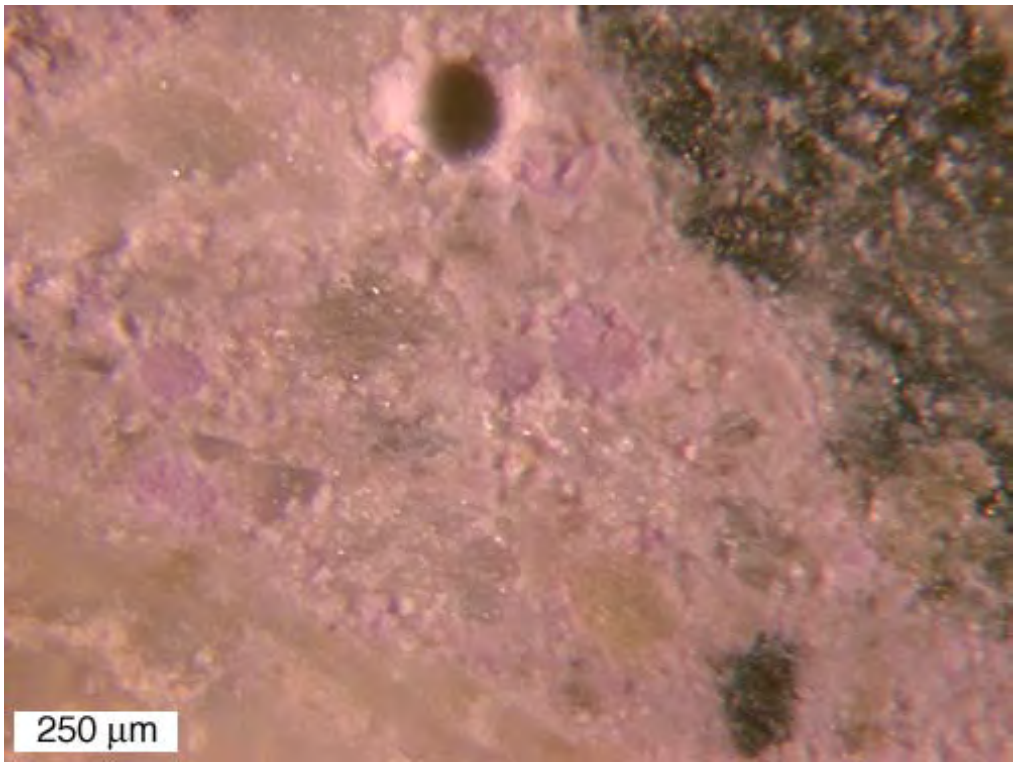

Figure D-64. Pink stained ettringite deposits in entrained air voids, Core 12-B.

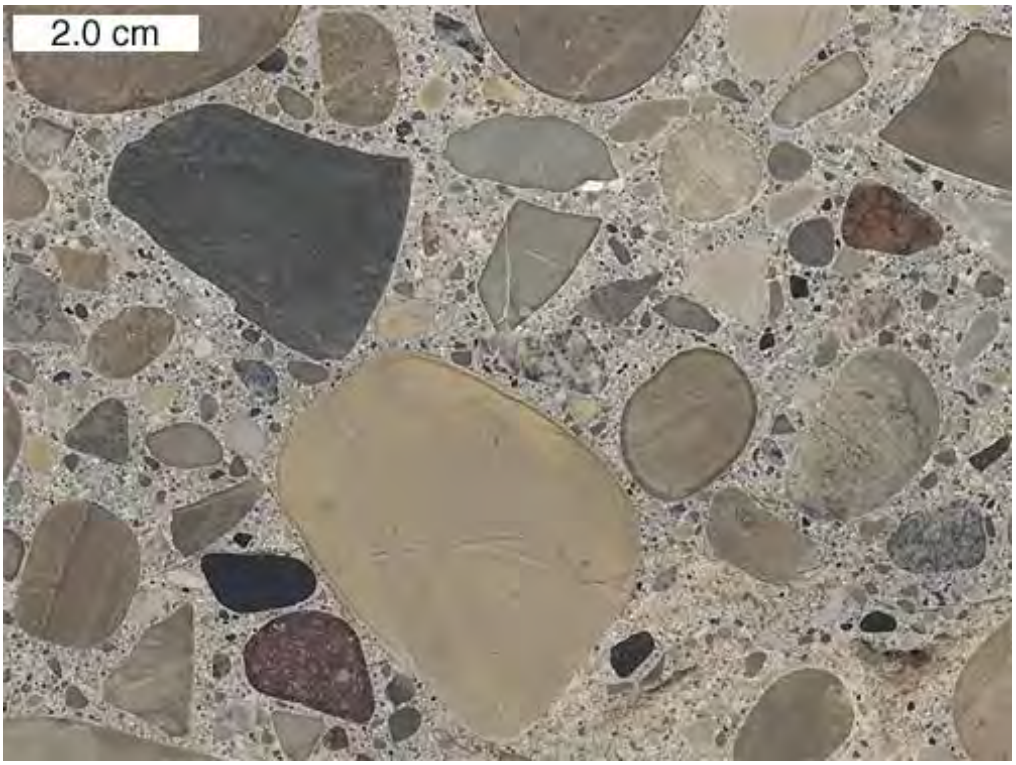

Figure D-65a. View of polished slab with cracked carbonate coarse aggregates, Core 22-B.

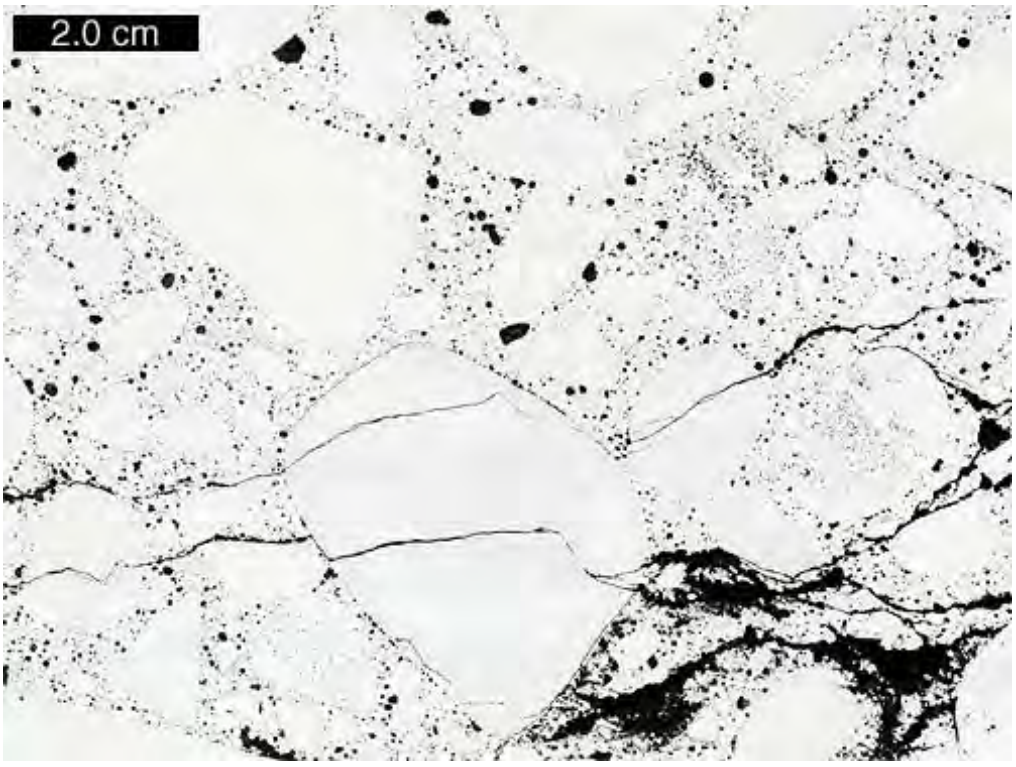

Figure D-65b. Negative image of area shown in Figure 7a after painting surface black and pressing with white powder to enhance cracks, Core 22-B.

Figure D-66a. View of polished slab with cracked carbonate coarse aggregates, Core 12-B.

Figure D-66b. Negative image of area shown in Figure 8a after painting surface black and pressing with white powder to enhance cracks, Core 12-B.

pink. Over time, such minerals commonly occur as secondary growths in the entrained air voids. Often, entrained air voids in deteriorated concrete are completely filled with secondary ettringite. The stain assists in the identification of filled air voids that may otherwise be mistaken for hardened cement paste. In the equations used to determine the air-void system parameters, filled air voids that are identified as paste would be considered to offer no protection to freeze-thaw damage. It is controversial whether filled air voids can protect the paste against freeze-thaw damage, and thus, air-void system parameters are computed for both the concrete in its original state, and the concrete in its existing state. Table D-12 shows the results of the Modified Point-Count for the five sites. Figure D-67 plots the spacing factors for each site, along with dotted lines to represent the suggested range according to ASTM C457. Figure D-68 plots the void frequency for each site, along with dotted lines to represent the suggested range according to ASTM C457. Figure D-69 compares the aggregate, cement paste and air volume percentages as determined by point count to the volume percentages computed from the mix design.

CONCLUSIONS

Test Site Nos. 12, 22, and 28 were from distressed pavements made with natural gravel coarse aggregate. Two of these test sites were built in 1957, and the third in 1960, so they are over 40 years old, and were still in service at the time of inspection. It seems likely that these pavements would have continued in service for many more years if it were not for the MRD. In general, compared to the typical concrete mixture used today, the concrete mixtures have a low cement content and large maximum aggregate size. The results of the microstructural evaluation can be summarized as follows:

- Unlike the concrete in the test sites containing slag coarse aggregate, the fine aggregate chert constituents, although showing signs of reactivity, have not reacted in a deleterious fashion. There is no cracking associated with these fine chert particles.
- On the other hand, coarse aggregate chert particles present in the natural gravel used in Test Site Nos. 12 and 28 do show signs of being deleteriously reactive, being linked both to alkali-silica reaction product and cracking. These same aggregates have properties that would make them potentially susceptible to aggregate freeze-thaw deterioration.
- The large coarse aggregate carbonates particles are porous and show significant cracking in the vicinity of joints. These are classic “D-crackers”, having all the diagnostic features of suffering aggregate freeze-thaw deterioration.

Table D-12. Results of ASTM C457 Modified Point Counts.

MTU Core ID	**12-B**	**22-D**	**28-C**
Raw Data			
area analyzed (cm^2)	90.5	156.9	152.6
air stops	136	98	139
paste stops	471	302	239
aggregate stops	1156	1154	1128
secondary ettringite stops	5	10	15
total stops	1768	1564	1521
traverse length (mm)	4618	5720	5564
# of air void intercepts	1752	1278	1819
# of secondary ettringite filled intercepts	113	92	14
Results			
vol% aggregate	65.4	73.8	74.2
vol% air original	8.0	6.9	10.1
vol% air existing	7.7	6.3	9.1
vol% paste original	26.6	19.3	15.7
vol% paste existing	26.9	19.9	16.7
original void frequency (voids/m)	404	240	329
existing void frequency (voids/m)	379	223	327
original avg. chord length (mm)	0.197	0.288	0.307
existing avg. chord length (mm)	0.203	0.280	0.280
original specific surface (mm^{-1})	20.3	13.9	13.0
existing specific surface (mm^{-1})	19.7	14.3	14.3
original paste/air ratio	3.3	2.8	1.6
existing paste/air ratio	3.5	3.2	1.8
original spacing factor (mm)	0.165	0.202	0.119
existing spacing factor (mm)	0.177	0.223	0.128

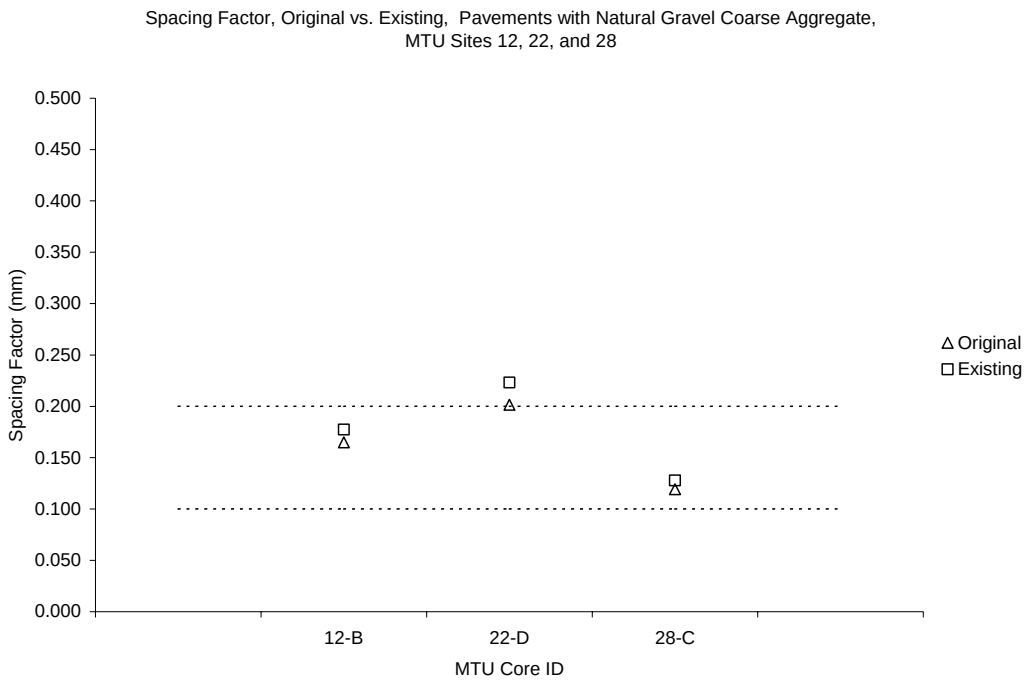

Figure D-67. Spacing factors plotted with dotted lines showing suggested values from ASTM C457.

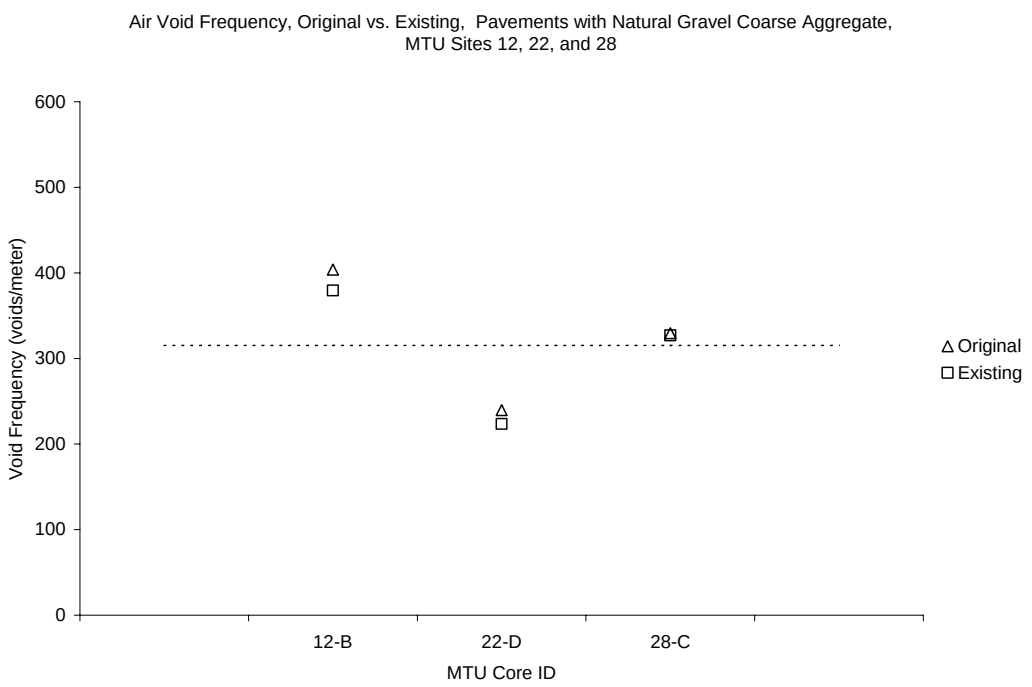

Figure D-68. Void frequencies plotted with dotted lines showing suggested values from ASTM C457.

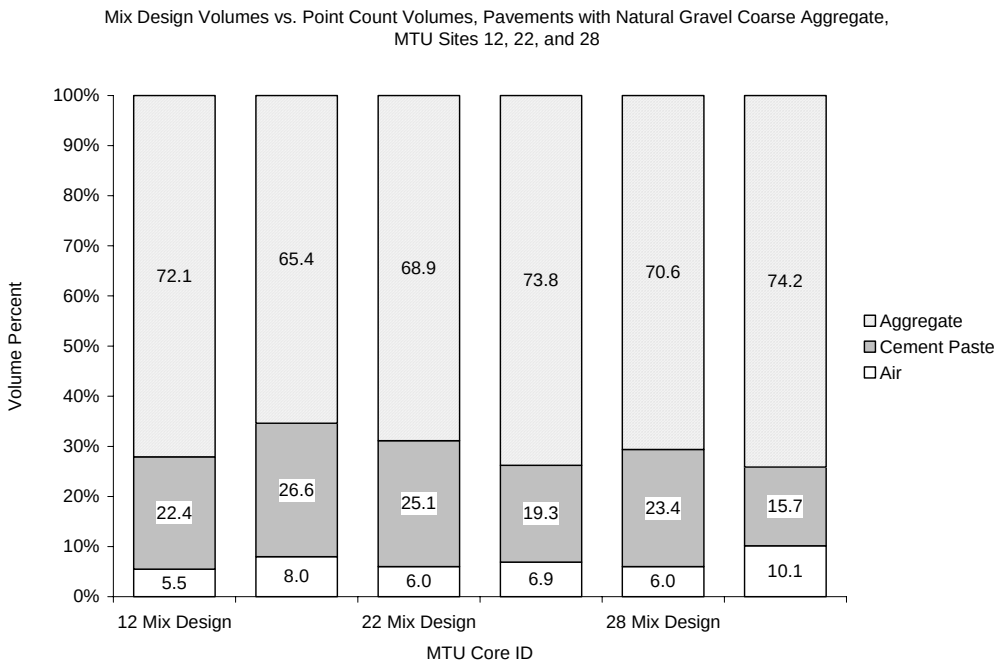

Figure D-69. Volume percentages from point counts compared to volume percentages computed from mix designs.